Monthly Notices
of the
ROYAL ASTRONOMICAL SOCIETY

MNRAS **512,** 989–1002 (2022)
Advance Access publication 2022 March 3

https://doi.org/10.1093/mnras/stac537

The ALMA REBELS survey: the dust content of $z \sim 7$ Lyman break galaxies

P. Dayal [1★] A. Ferrara,[2] L. Sommovigo,[2] R. Bouwens,[3] P. A. Oesch,[4,5] R. Smit,[6] V. Gonzalez,[7,8] S. Schouws,[3] M. Stefanon [3], C. Kobayashi [9], J. Bremer,[1] H. S. B. Algera,[10] M. Aravena,[11] R. A. A. Bowler [12], E. da Cunha,[13,14] Y. Fudamoto [4,15,16], L. Graziani [17,18] J. Hodge,[19] H. Inami,[10] I. De Looze,[20,21] A. Pallottini [2], D. Riechers,[22] R. Schneider [17,23,24,25] D. Stark[26] and R. Endsley [26]

Affiliations are listed at the end of the paper

Accepted 2022 February 22. Received 2022 February 22; in original form 2021 November 2

ABSTRACT

We include a fully coupled treatment of metal and dust enrichment into the DELPHI semi-analytic model of galaxy formation to explain the dust content of 13 Lyman break galaxies (LBGs) detected by the Atacama Large millimetre Array (ALMA) REBELS Large Program at $z \simeq 7$. We find that the galaxy dust mass, $M_{\rm d}$, is regulated by the combination of Type II supernova dust production, astration, shock destruction, and ejection in outflows; grain growth (with a standard time-scale $\tau_0 = 30$ Myr) plays a negligible role. The model predicts a dust-to-stellar mass ratio of ~ 0.07–0.1 per cent and a UV-to-total star formation rate relation such that $\log(\psi_{\rm UV}) = -0.05\,[\log(\psi)]^2 + 0.86\,\log(\psi) - 0.05$ (implying that 55–80 per cent of the star formation is obscured) for REBELS galaxies with stellar mass $M_* = 10^9$–$10^{10}{\rm M}_\odot$. This relation reconciles the intrinsic UV luminosity of LBGs with their observed luminosity function at $z = 7$. However, 2 out of the 13 systems show dust-to-stellar mass ratios (~ 0.94–1.1 per cent) that are up to 18 times larger than expected from the *fiducial* relation. Due to the physical coupling between dust and metal enrichment, even decreasing τ_0 to very low values (0.3 Myr) only increases the dust-to-stellar mass ratio by a factor of $\sim$2. Given that grain growth is not a viable explanation for such high observed ratios of the dust-to-stellar mass, we propose alternative solutions.

Key words: dust, extinction – galaxies: evolution – galaxies: high-redshift – galaxies: ISM – galaxies: luminosity function, mass function.

1 INTRODUCTION

Over the past decade instruments such as the *Hubble Space Telescope* (*HST*), Very large Telescope (VLT), *Subaru*, and *Keck* have been used to assemble statistically large sample of high-redshift ($z \gtrsim 5$) Lyman break galaxies (LBGs) at rest-frame ultraviolet (UV) wavelengths. These have provided excellent constraints on the key physical properties of early galaxies including the evolving UV luminosity function (UV LF), stellar mass function (SMF), and the redshift evolution of the star formation rate (SFR) density and stellar mass density, to name a few (see reviews by e.g. Dunlop 2013; Stark 2016; Dayal & Ferrara 2018).

However, the impact of dust, which absorbs UV and optical photons that are re-emitted at Far Infra-red (FIR) wavelengths and can severely impact the UV-detectability of galaxies (Draine 2003), remained an open question especially at $z \gtrsim 5$. The advent of instruments such as the Plateau de Bure Interferometer (PdBI) and the Atacama Large millimetre Array (ALMA) have opened up a new window on the dust content of such early star forming galaxies (for a review see Hodge & da Cunha 2020). Indeed, FIR observations have now been used to estimate dust-to-stellar mass ratios ranging between 0.012 and 3 per cent for 'normal' star forming galaxies, with stellar masses $M_* \sim 10^{8.3}$–$10^{10.5}{\rm M}_\odot$, at $z \gtrsim 7$ (e.g. Watson et al. 2015; Laporte et al. 2017; Marrone et al. 2018; Hashimoto et al. 2019; Bakx et al. 2020; Reuter et al. 2020; Fudamoto et al. 2021; Schouws et al. 2021).

These have been complemented by a range of theoretical models aimed at understanding the key dust processes and their resulting impact on the visibility of galaxies. A number of zoom-in simulations have been crucial in understanding the role of a range of interstellar medium (ISM) processes – such as dust growth and dissociation, supernova (SN) shock destruction, ISM dust grain growth, and gas drag effects – on the dust distribution and its grain-size distribution in individual galaxies (Bekki 2015; Aoyama et al. 2017; McKinnon et al. 2018). These have been supplemented by hydrodynamic simulations have both been post-processed citep-dayal2011, mancini2015, narayanan2018, wilkins2018, ma2019, vogelsberger2020, vijayan2021 and coupled with dust models (Li, Narayanan & Davé 2019; Graziani et al. 2020; Kannan et al. 2021) to obtain the dust masses and resulting attenuation relations for high-redshift galaxies. Finally, a number of semi-analytic models have been constructed to study the impact of different processes on the dust content of high-z galaxies (Popping, Somerville & Galametz 2017; Vijayan et al. 2019; Triani et al. 2020).

★ E-mail: p.dayal@rug.nl

A key issue in determining the dust masses of early galaxies is that the observed FIR continuum emission is characterized by key two quantities – the dust temperature (T_d) and the dust mass (M_d). Unless multiband dust measurements are available (see e.g. Faisst et al. 2020; Bakx et al. 2021), these two quantities are degenerate, requiring an assumption on the dust temperature in order to infer the associated dust mass. This has led to two classes of explanations for the exceedingly high dust-to-stellar mass ratios seen for $z \gtrsim 7$ galaxies: the first focuses on invoking extremely fast grain growth in the ISM (e.g. Mancini et al. 2015; Michałowski 2015). The second is that the (luminosity-weighted) dust temperatures are, in fact, significantly higher – up to ≈90 K (Behrens et al. 2018; Sommovigo et al. 2020) – than the usually assumed values of ∼35–40 K (see also Shen et al. 2021; Vijayan et al. 2021). Given that the FIR luminosity scales as $L_{\rm FIR} \propto M_d T_d^6$, this reduces the inferred dust mass by 2.1–2.5 orders of magnitude, thus removing the need to invoke extreme grain growth rates that appear to be problematic at high redshifts (Ferrara 2016).

In order to build a larger sample of dusty star forming galaxies at high-z, an ALMA large program (the Reionization Era Bright Emission Line Survey; REBELS; PI: Bouwens) is underway. REBELS focuses on studying 40 of the brightest galaxies at $z \gtrsim 6.5$ over a 7 deg^2 area that are being scanned for both bright ISM cooling lines (such as those from [C II] 158 μm and [O III] 88 μm) and dust continuum emission, as detailed in Bouwens et al. (2022). This survey has already serendipitously revealed two dusty star forming galaxies at $z \sim 7$ (Fudamoto et al. 2021) in addition to yielding a sample of 13 (continuum and C II detected) $z \sim 7$ LBGs (Inami et al., in preparation; Schouws et al., in preparation) with $M_* \sim 10^{8.8}$–$10^{10.6}$M$_\odot$ (Stefanon et al., in preparation; Topping et al., in preparation) and dust masses of $M_d \sim 10^{6.8}$–$10^{7.5}$M$_\odot$ (Sommovigo et al. in preparation); the associated dust-to-stellar mass ratios range within ∼ 0.2–1.1 per cent.

In this work, our goal is to (i) study the key processes determining the dust content of high-redshift ($z \gtrsim 7$) LBGs; and (ii) explore the impact of different ISM grain-growth time-scales on the dust masses and UV-observability of such galaxies. To this end, we augment our DELPHI[1] semi-analytic model with a detailed treatment of chemical and dust enrichment in the ISM of LBGs. Although similar in spirit to the semi-analytic models noted above (e.g. Popping et al. 2017; Vijayan et al. 2019; Triani et al. 2020), the key strengths of this work lie in the fact that (i) it uses a minimal number (two) of mass- and redshift-independent free parameters to model the key physics of early galaxies; and (ii) contrary to the other models that have been calibrated against low-redshift ($z \sim 0$–3) data, our model has been calibrated against all available data sets for $z \gtrsim 5$ galaxies including the evolving UV LF and SMF. Once calibrated against these, our model also reproduces the observed redshift evolution of the SFR density and stellar mass density, to note a few; and (iii) this is the only semi-analytic model that includes the latest state-of-the-art yields from Type Ia SN (SN Ia), Type II SN (SN II), and asymptotic giant branch (AGB) stars from Kobayashi, Karakas & Lugaro (2020) so far. This yield set can reproduce the observations not only for oxygen but also for most of all stable elements (up to uranium) self-consistently.

We adopt a ΛCDM model with dark energy, dark matter and baryonic densities in units of the critical density as $\Omega_\Lambda = 0.691$, $\Omega_m = 0.308$, and $\Omega_b = 0.049$, respectively, a Hubble constant $H_0 = 100\,h\,{\rm km\,s^{-1}\,Mpc^{-1}}$ with $h = 0.67$, spectral index $n = 0.96$, and normalization $\sigma_8 = 0.81$ (Planck Collaboration XLVII 2016).

[1]**D**ark Matter and the **e**mergence of ga**l**axies in the e**p**oc**h** of re**i**onization.

Throughout this work, we use a Salpeter initial mass function (IMF; Salpeter 1955) within 0.1–100 M$_\odot$ and a mass-weighted solar metallicity value of $Z_\odot = 0.0122$ (Asplund, Grevesse & Sauval 2005). Finally, we quote all quantities in comoving units, unless stated otherwise, and express all magnitudes in the standard AB system (Oke & Gunn 1983).

We describe the DELPHI model in Section 2 before discussing the metal and dust models and their implementation in Section 2.1 and the rate evolution of the key dust processes in Section 2.2. We show the dust masses, dust-to-gas ratios, and dust-to-metal mass ratios for $z \sim 7$ LBGs in Section 3. We then explore the effects of dust attenuation on the UV LF in Section 4.1 and on the UV-to-total SFR relation in Section 4.2 before concluding in Section 5.

2 MODEL

We start by briefly describing the DELPHI model and interested readers are referred to Dayal et al. (2014) for complete details. DELPHI uses a binary merger tree approach to jointly track the build-up of dark matter haloes and their baryonic components (both gas and stellar mass). We start by building merger trees for 600 galaxies at $z = 4.5$, uniformly distributed in the halo mass range of $\log(M_h/{\rm M}_\odot) = 8 - 14$, up to $z = 40$ in equal time-steps of $\Delta t = 30$ Myr. This value is chosen so that all SN II from a given single stellar population explode within the same time-step (SN II progenitors have lifetimes of $\lesssim 28$ Myr; Padovani & Matteucci 1993). Each $z = 4.5$ halo is assigned a co-moving number density by matching the dn/dM_h value of the $z = 4.5$ Sheth–Tormen halo mass function (HMF; Sheth & Tormen 1999) and this number density is propagated throughout the merger tree of that halo. Thus, the resulting HMFs comply with the Sheth–Tormen one at all z.

The very first progenitors of every $z = 4.5$ halo, that mark the start of its assembly ('starting leaves'), are assigned an initial gas mass according to the cosmological baryon-to-dark matter ratio such that $M_g^i = (\Omega_b/\Omega_m)M_h$. For haloes that have progenitors, the halo mass is built via merging progenitors as well as smooth accretion of dark matter from the intergalactic medium (IGM). The initial gas mass in this case is the sum of the final gas mass inherited from its progenitors and that gained via smooth accretion making the *Ansatz* that accretion of dark matter is accompanied by accretion of a cosmological fraction (Ω_b/Ω_m) of gas mass. A fraction of this initial gas mass is converted into stars with an effective star formation efficiency $f_*^{\rm eff} = \min[f_*^{\rm ej}, f_*]$, i.e. the minimum between (a) the efficiency that produces enough SN II energy to unbind the remainder of the gas ($f_*^{\rm ej}$), and (b) an upper maximum threshold, f_* (see below).

We compute the newly formed stellar mass at any z as $M_*(z) = M_g^i(z) f_*^{\rm eff}$; the corresponding SFR is $\psi(z) = M_*(z)/\Delta t$. This star formation can impart the ISM with a total SN II energy given by $E_{\rm SN} = f_w E_{51} \nu M_*(z)$, where f_w is the fraction of SN II energy that couples to the gas, $E_{51} = 10^{51}$erg is the instantaneous energy produced per SN II and ν is the SN II rate per unit stellar mass formed; our chosen Salpeter IMF within 0.1–100 M$_\odot$ results in $\nu^{-1} = 134\,{\rm M}_\odot$. Further, at each step, we update the gas mass, including that lost in star formation and SN feedback. We also account for the gas return fraction (R) – this is the gas returned by exploding stars to the ISM for which we use the mass- and metallicity-dependent yields presented in Kobayashi et al. (2020). At the end of a redshift step z, the final gas mass is

$$M_g^f(z) = [M_g^i(z) - M_*(z)]\left(1 - \frac{f_*^{\rm eff}}{f_*^{\rm ej}}\right) + R M_*(z), \quad (1)$$

and the ejected gas mass is

$$M_{\rm g}^{\rm eje}(z) = [M_{\rm g}^{\rm i}(z) - M_*(z)]\left(\frac{f_*^{\rm eff}}{f_*^{\rm ej}}\right). \quad (2)$$

Each newly formed stellar population is assigned the metallicity of the ISM (computed as detailed in Section 2.1 that follows) at the previous time-step and assumed to have an age of 2 Myr. These parameters are used in conjunction with the population synthesis code STARBURST99 (Leitherer et al. 1999) to obtain the specific UV luminosity at $\lambda = 1500$ Å expressed as L_{1500} (erg s^{-1} Hz^{-1}).[2] The total UV luminosity is the sum of this value plus the time-decayed UV luminosity from all older stellar populations in the galaxy.

Associated REBELS papers use a conversion between the UV luminosity and the SFR such that $L_{1500} = \psi\kappa^{-1}$. While the REBELS collaboration uses a value of $\kappa = 7.1 \times 10^{-29}$ ($M_\odot$ yr^{-1} erg^{-1} s Hz) based on a Chabrier IMF (0.1–300$M_\odot$), the paper inferring the UV SFR values (Ferrara et al. 2022) uses a value of $\kappa = 4.45 \times 10^{-29}$ based on a Salpeter IMF (1–100$M_\odot$). Averaged over REBELS mass galaxies ($M_* \sim 10^9$–$10^{10}M_\odot$), we find a value of $\kappa = 8.9 \times 10^{-29}$ based on our Salpeter IMF (0.1–100 $M_\odot$). In what follows, all inferred SFRs for REBELS sources are re-calibrated to our IMF and summarized in Table 2.

We note that our model contains only two mass- and redshift-independent free parameters to match to observations. These are (a) the maximum (instantaneous) star formation efficiency of $f_* =$ 8 per cent; and (b) the fraction $f_w (\approx 7.5$ per cent) of the SN II explosion energy that is available to drive an outflow. These parameters have been tuned to simultaneously reproduce the observed SMF (from González et al. 2011; Duncan et al. 2014; Song et al. 2016), and the UV LF at $z \sim 5$–12 (from e.g. Castellano et al. 2010; McLure et al. 2013; Atek et al. 2015; Finkelstein et al. 2015; Bouwens et al. 2016; Calvi et al. 2016; Bowler et al. 2017; Livermore, Finkelstein & Lotz 2017; Ishigaki et al. 2018; Oesch et al. 2018; Harikane et al. 2022; Bouwens et al. 2021). While f_* is crucial in determining the high-mass end of the SMF, f_w determines the low-luminosity and low-mass ends of the UV LF and SMF, respectively (Dayal et al. 2014).

2.1 Modelling the dust and metal contents of high-redshift galaxies

The dust and metal contents of galaxies are inextricably interlinked. Dust and metals are produced by both SNe and evolved AGB stars. However, AGB stars contribute only a few per cent to the total dust mass for $z \gtrsim 5$ LBGs (e.g. Dayal, Ferrara & Saro 2010; Mancini et al. 2015; Leśniewska & Michałowski 2019), given their long evolutionary time-scales. Whilst accounting for metals produced by both SN II and AGB, for the sake of simplicity, in this work, we assume that dust in $z \gtrsim 5$ LBGs is solely produced by SN II. We include the key processes of metals and dust production, astration, ejection and dust destruction and grain growth in the ISM. Given a lack of spatial information, we assume gas accreted from the IGM to be devoid of both metals and dust. However, as detailed in what follows, we do consider models without any ejection of metals and dust – in principle, their results would be comparable to a model wherein all ejected gas and metals stay in the circumgalactic medium and can be re-accreted at a later time-step. The evolution of the dust and the *gas-phase* metal masses as a function of time (or, equivalently, redshift) is described in detail in what follows.[3] In our calculation, the *total* metal mass at any redshift is the sum of the gas-phase metal mass and the dust mass.

If a galaxy has no progenitors, we assume both the initial metal and dust masses to be zero, i.e. $M_{\rm Z}^i(z) = 0$ and $M_{\rm d}^i(z) = 0$, respectively. On the other hand, for a galaxy with progenitors, the metal and dust masses at redshift z are the sum of the metals and dust brought in by all the progenitors from previous time-steps. At each time-step, DELPHI solves the following differential equation to calculate the change in the *gas-phase* metal mass using the instantaneous recycling approximation (IRA; Tinsley 1980) as

$$\frac{{\rm d}M_{\rm Z}}{{\rm d}t} = \dot{M}_{\rm Z}^{'\rm pro} - \dot{M}_{\rm Z}^{\rm ast} + \dot{M}_{\rm d}^{\rm des} - \dot{M}_{\rm Z}^{\rm eje} - \dot{M}_{\rm d}^{\rm gro}. \quad (3)$$

The five terms on the right-hand side are the rates of:

(i) *Metal production*: The first term, $\dot{M}_{\rm Z}^{'\rm pro}$ is the rate of gas-phase metal enrichment. It is calculated as $\dot{M}_{\rm Z}^{'\rm pro} = \dot{M}_{\rm Z}^{\rm pro} - \dot{M}_{\rm d}^{\rm pro}$, where the first term on the right-hand side shows the mass- and metallicity-dependent yields for stars between 0.1 and 50 $M_\odot$ using the results presented in Kobayashi et al. (2020); larger mass stars are assumed to collapse to black holes without producing any metals. The second term shows the rate at which dust condenses out of these metals, reducing the gas-phase metal content. This latter term is discussed in detail in what follows.

(ii) *Metal astration*: the assimilation of a homogeneous mixture of metals into stars, which is expressed as $\dot{M}_{\rm Z}^{\rm ast} = [M_{\rm Z}/M_{\rm g}]\psi(t)$.

(iii) *Dust destruction*: the dust mass that is destroyed in SN II shocks, $M_{\rm d}^{\rm des}$, adds to the metal mass in the ISM. This term is detailed in what follows.

(iv) *Ejection*: of perfectly mixed metal-enriched gas in outflows such that $\dot{M}_{\rm Z}^{\rm eje} = [M_{\rm Z}/M_{\rm g}]\dot{M}_g^{\rm eje}$. We assume the ejected gas is homogeneously ejected over the entire time-step so that $\dot{M}_g^{\rm eje} = M_{\rm g}^{\rm eje}/\Delta t$.

(v) *Depletion*: this accounts for ISM metals lost to dust grain growth in the cold ISM. This term, $\dot{M}_{\rm d}^{\rm gro}$, is also detailed in what follows.

Similarly, at each time-step, the dust mass is calculated solving the equation

$$\frac{{\rm d}M_{\rm d}}{{\rm d}t} = \dot{M}_{\rm d}^{\rm pro} - \dot{M}_{\rm d}^{\rm ast} - \dot{M}_{\rm d}^{\rm des} - \dot{M}_{\rm d}^{\rm eje} + \dot{M}_{\rm d}^{\rm gro}. \quad (4)$$

The five terms on the right-hand side are the rates of the physical processes governing dust abundance:

(i) *Dust production*: by SN II is written as $\dot{M}_{\rm d}^{\rm pro} = y_{\rm d}\nu\psi(t)$, where $y_{\rm d} = 0.5\,M_\odot$ is the adopted dust yield per SN II (e.g. Todini & Ferrara 2001; Bianchi & Schneider 2007). This value is also in agreement with the dust yields ranging between 0.03 and 1.1 $M_\odot$ inferred from observations of SN in the local Universe (e.g. Matsuura et al. 2015; Temim et al. 2017; Rho et al. 2018; Priestley et al. 2020; Niculescu-Duvaz et al. 2021). However, a long-standing question is how much of this dust can escape into the ISM, due to the destruction by the reverse shock (see e.g. Bocchio et al. 2016; Slavin et al. 2020).

(ii) *Dust destruction*: by SN II shocks is expressed as

$$\dot{M}_{\rm d}^{\rm des} = (1 - X_{\rm c})\tau_{\rm des}^{-1}\mathcal{D}, \quad (5)$$

where $\mathcal{D} = M_{\rm d}/M_{\rm g}$ is the dust-to-gas ratio and $(1 - X_{\rm c})$ is the mass fraction of warm ISM where dust can be destroyed. We use a fiducial

[2]The specific UV luminosity includes both the stellar emission and nebular continuum with the latter contributing ∼15 per cent to the luminosity value.

[3]For the purposes of this work, we only track the total metal and dust masses, without tracking individual metal species.

value of $X_c = 0.5$, based on recent high-z galaxy simulation results (Pallottini et al. 2019). The dust destruction time-scale is

$$\tau_{\rm des}^{-1} = f\,\epsilon\,\nu\,\psi\,M_{\rm s}, \quad (6)$$

where ϵ is the dust destruction efficiency by shocks for which we use a value of 0.2 (Seab & Shull 1983; McKee 1989),[4] f is the fraction of SN II that contribute to such shocks for which we use a value of 0.15 (de Bennassuti et al. 2014) and $M_{\rm s}(100\,{\rm km\,s^{-1}}) = 6.8\times10^3\,{\rm M_\odot}$ is the mass accelerated to >100 km s^{-1} by the SN blast wave (McKee 1989; Lisenfeld & Ferrara 1998). These values yield $f\epsilon = 0.03$ and $\dot{M}_{\rm d}^{\rm des} = 0.76\mathcal{D}\psi(t)$.

(iii) *Dust astration*: is simply written as $\dot{M}_{\rm d}^{\rm ast} = \mathcal{D}\psi(t)$ where we assume astration of perfectly mixed gas and dust from the ISM.

(iv) *Dust ejection*: with the same hypothesis of perfect mixture, is $\dot{M}_{\rm d}^{\rm eje} = \mathcal{D}\dot{M}_{g}^{\rm eje}$.

(v) *Grain growth*: occurs by accretion of heavy elements in the cold ISM component. An increase in the dust mass due to ISM growth must therefore be equalled by a decrease in the metal mass. This is modelled as (Dwek 1998)

$$\dot{M}_{\rm d}^{\rm gro} = \left(1 - \frac{M_{\rm d}}{M_Z + M_{\rm d}}\right)\frac{X_{\rm c}M_{\rm d}}{\tau_{\rm acc}}, \quad (7)$$

where the first term ensures that the dust mass does not exceed the total metal mass and $\tau_{\rm acc}$ is the grain growth time-scale. A simple expression for the latter quantity is $\tau_{\rm acc} = \tau_0(Z/Z_\odot)^{-1}$, where Z is the gas-phase metallicity ($=M_z/M_g$) and τ_0 is a scaling time-scale for which we explore values between 0.3 and 30 Myr. Our τ_0 values have been chosen in order to encompass the grain growth time-scales explored in a number of other theoretical works (e.g. Mancini et al. 2015; Popping et al. 2017; Vijayan et al. 2019; Graziani et al. 2020; Triani et al. 2020) up to the time difference between consecutive merger-tree steps.

We also calculate an (unphysical) upper limit to the dust mass ($M_{\rm d}^{\rm max}$) considering the processes of dust production (assuming a yield of $y_{\rm d} = 1{\rm M_\odot}$), astration, and growth assuming $\tau_0 = 0.3$ Myr; dust is neither destroyed nor ejected in outflows in this case. This *gedankenexperiment* is termed the 'maximal dust mass model' and its implications are discussed in Sections 3 and 4.

Using a single grain size and material density of $a = 0.05\,\mu$m and $s = 2.25\,{\rm g\,cm^{-3}}$ appropriate for graphite/carbonaceous grains, respectively (Todini & Ferrara 2001; Nozawa et al. 2003), this dust mass can be used to compute the ISM optical depth, $\tau_{\rm c}$, to UV continuum photons as $\tau_{\rm c} = 3M_{\rm d}[4\pi r_g^2 as]^{-1}$; we have assumed the extinction cross-section of the grains to be $Q_{\rm ext} \approx 1$ at 1500 Å. Further, we have assumed dust and gas to be co-spatially distributed within the gas radius $r_g = 4.5\lambda r_{\rm vir}$ (Ferrara, Pettini & Shchekinov 2000). We take the spin parameter $\lambda = 0.04$ (Davis & Natarajan 2009; Dayal & Ferrara 2018), where $r_{\rm vir}$ is the virial radius of the halo at the considered redshift.

This optical depth can be easily converted into a value for the escape fraction of continuum photons, $f_{\rm c}$, by modelling the disc as a slab in which dust and stars are intermixed. This yields

$$f_{\rm c} = \frac{1 - {\rm e}^{-\tau_{\rm c}}}{\tau_{\rm c}}, \quad (8)$$

which for small optical depths is $\sim$1. Note that $1 - f_{\rm c}$ can be also interpreted as the fraction of obscured SFR in the galaxy.

[4]The predicted range of ϵ ranges between 0.1 and 0.5, with the precise value depending on the ISM density and magnetic field strength.

The above equations have been implemented in DELPHI, and solved self-consistently with cosmological galaxy evolution. In the following, we will refer to the dust mass calculated with a grain growth time-scale of $\tau_0 = 30$ Myr as the *fiducial* model. The key model-free parameters and their values are summarized in Table 1.

2.2 Rate evolution of key dust processes

We start by clarifying the relative role of the different processes discussed in equation (4) in shaping the dust content of early galaxies. To do this, we show the redshift evolution of the rate associated with each dust process, averaged over 'REBELS mass' galaxies with $M_* \sim 10^9$–$10^{10}{\rm M_\odot}$ at $z \simeq 7$, in Fig. 1. In the *fiducial* scenario ($\tau_0 = 30$ Myr, left-hand panel), such galaxies have a dust mass of $M_{\rm d} \sim 10^{6.6}{\rm M_\odot}$ by $z \sim 7$ with dust production dominating the dust mass assembly at all redshifts. Given their dependence on $\mathcal{D}$, the sum of the astration and destruction rates increase with $M_{\rm d}$ (and hence, redshift) from being ≈ 26 per cent of the production rate at $z \sim 12$ to ≈ 40 per cent by $z \sim 7$. While the ejection rate also increases with time (given it is also $\propto \mathcal{D}$), its slope becomes shallower with decreasing redshift. This is because as haloes grow in mass, the rate of gas and dust ejection decreases. Indeed, the ejection rate decreases from being about ≈ 67 per cent of the production rate at $z \sim 12$ to ≈ 44 per cent by $z \sim 7$. Finally, the ISM grain growth rate increases with metallicity, from about 1.4 per cent of the production rate at $z \sim 12$ to 8 per cent by $z \sim 7$. As seen, the total rate of dust growth shows a sharp decline at $z \gtrsim 12$ where the production rate is essentially balanced by the rates of dust astration, destruction, and ejection. By $z \sim 7$, astration, destruction and ejection add up to about 84 per cent of the production rate, with grain growth playing a sub-dominant role. In this *fiducial* case, the redshift-evolution of the total dust mass for $M_* \sim 10^9$–$10^{10}{\rm M_\odot}$ galaxies follows a roughly linear relation such that

$$\log M_{\rm d} = -0.33z + 8.9. \quad (9)$$

As seen from Fig. 1, ejection is the dominant mechanism responsible for decreasing the dust mass in the early assembly ($z \gtrsim 12$) of 'REBELS-mass' galaxies. Since our model assumes ejection of perfect mixed dust, gas-phase metals and gas, it results in the same fractional mass ejection of dust and metals. However, given the larger production rates (from both AGB and SN II) for metals and the fact that at any given time, dust destruction adds to the gas-phase metal mass, the rate of metal mass growth is less affected by ejection even at the highest redshifts, resulting in a high dust-to-metal mass. As these galaxies build-up their halo mass and the impact of ejection decreases at $z \lesssim 10$, the rate of dust and metal growth start show similar slopes. This results in the dust mass-to-metal mass ratio decreasing with decreasing redshift. As shown in the same panel, $M_{\rm d}/M_z$ decreases from ~ 60 per cent at $z \sim 12$ to ~ 47 per cent by $z \sim 7$, with the metal mass being of the order $M_Z \sim 10^7{\rm M_\odot}$ by $z \sim 7$.

We then study the case where the grain growth time-scale is a factor hundred shorter ($\tau_0 = 0.3$ Myr, right-hand panel of the same figure); we note that in our formalism, the growth rate is regulated by the ratio of the dust and metal contents (Eqn. 7). In this case too, the dust production term dominates at all z. Although the shorter grain growth time-scales lead to a steeper increase in the total rate of dust growth and the associated dust mass with redshift as compared to the *fiducial* model, as a result of being modulated by the gas-phase metal mass, the final dust mass is only a factor 1.5 larger ($M_{\rm d} \sim 10^{6.75}{\rm M_\odot}$) by $z \sim 7$. As it might be expected, the steeper build-up of dust mass also results in the astration + destruction and ejection rates showing a steeper slope (through their dependence on $\mathcal{D}$). Indeed, by $z \sim 7$, the astration + destruction and ejection rates are roughly

Table 1. A summary of the key physical parameters for two of the theoretical models explored in this work.

Model	f_* (per cent)	f_w (per cent)	$y_d(M_\odot)$	X_c	Dust destruction	Dust astration	Dust ejection	$f\epsilon$	τ_0 (Myr)
Fiducial	8	7.5	0.5	0.5	yes	yes	yes	0.03	30
Maximal	8	7.5	1.0	0.5	no	yes	no	0.03	0.3

Note. For the model shown in column 1, we note the maximum instantaneous star formation efficiency (column 2), the fraction of SN II energy that couples to gas (column 3), the dust yield per SN II after SN shock processing (column 4), the fraction of warm ISM gas (column 5), whether the processes of dust destruction, astration, and ejection have been included (columns 6–8), the product of the dust destruction efficiency and the fraction of SN II contributing to such shocks (column 9), and the dust grain growth time-scale (column 10).

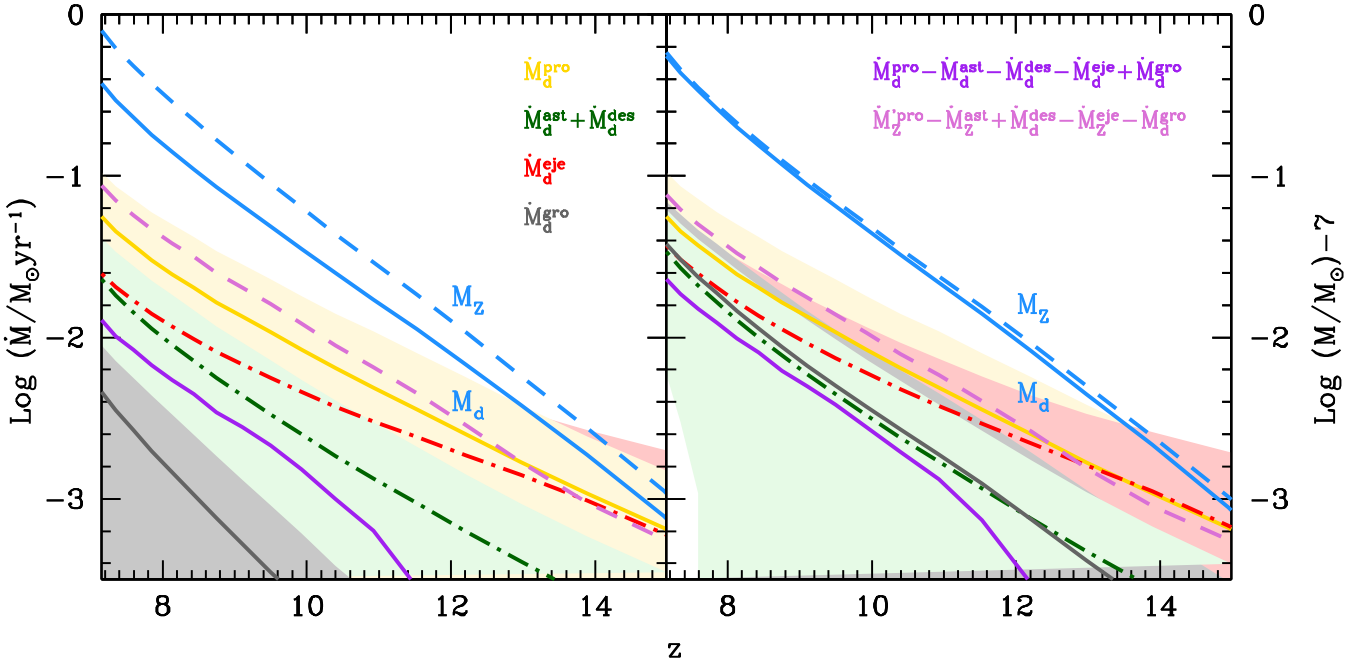

Figure 1. Redshift evolution of the rates of the key processes determining the dust mass for $M_* = 10^9$–$10^{10}M_\odot$ galaxies at $z \sim 7$ for two different grain growth time-scales (grey line): $\tau_0 = 30$ (left-hand panel) and 0.3 Myr (right-hand panel). The other lines show the (average values of the) different dust processes modelled: production (yellow), astration, and destruction (dark green) and ejection (red); the shaded regions show the 1σ errors for each line. In each panel, the solid and dashed blue lines show the total dust mass and metal mass scaled down by seven orders of magnitude, respectively. Finally, as marked in the right-hand panel, the solid purple and dashed violet lines in both panels show the total rate of dust and metal mass assembly, respectively.

60 per cent of the production rate. Further, a larger fraction of metals condensing into dust in this model results in a dust-to-metal ratio that increases with decreasing redshift, from about ≈ 82 per cent at $z \sim 18$ to ≈ 95 per cent by $z \sim 7$. In this model, the total metal content is almost equally split between gas-phase ISM metals and those bound up into dust.

To summarize, for $M_* \sim 10^9$–$10^{10}M_\odot$ galaxies at $z \sim 7$, the dust production rate dominates the dust build-up at all z for both the grain-growth time-scales considered here. In the *fiducial* model astration+destruction + ejection add up to ∼ 84 per cent of the production rate by $z \sim 7$, with grain growth playing a negligible role. However, invoking a model with $\tau_0 = 0.3$ Myr results in a steeper build-up of the dust mass resulting in a steeper rise in the astration + destruction and ejection rates; these processes each reach about 60 per cent of the production rate by $z \sim 7$.

3 THE DUST CONTENT OF HIGH REDSHIFT GALAXIES

We now briefly describe how quantities such as the dust mass, stellar mass and SFRs (UV and total) are derived for REBELS sources before these are compared to the model results. Interested readers are referred to Stefanon et al. (in preparation) and Topping et al. (in preparation) for complete details. The *fiducial* stellar masses for REBELS sources have been estimated from multiwavelength photometry using a version of BEAGLE (Chevallard & Charlot 2016) that incorporates nebular emission (both lines and continuum; Gutkin, Charlot & Bruzual 2016). We have assumed a constant star formation history (SFH), a metallicity value of $0.2Z_\odot$, a Calzetti dust extinction law (Calzetti et al. 2000), and a Chabrier IMF between 0.1 and $300M_\odot$ (Chabrier 2003). Additionally, Topping et al. (in preparation) have calculated the stellar masses adopting non-parametric SFHs[5] Further, the dust masses for the REBELS sources are derived in Sommovigo et al. (in preparation) using the method

[5]Using a Chabrier IMF, a metallicity of $0.2Z_\odot$ and a Small Magellanic Cloud (SMC) dust extinction law.. For the sources discussed in this work, the stellar masses derived by Topping et al. (in preparation) are, on average, 0.55 dex more massive than the values derived by Stefanon et al. (in preparation). In what follows, we primarily compare to the *fiducial* stellar masses derived by Stefanon et al. (in preparation) and comment on the differences with the Topping et al. (in preparation) results where appropriate.

Table 2. For the ID of the detected REBELS galaxies shown in column 1, we show the associated stellar mass (column 2), the luminosity weighted dust temperature (column 3), the dust mass (column 4), the UV SFR (column 5), and the total SFR (column 6).

Object	Redshift	$\log(M_*/\mathrm{M}_\odot)^a$	$T_\mathrm{d}(\mathrm{K})^b$	$\log(M_\mathrm{d}/\mathrm{M}_\odot)^c$	ψ_{UV} ($\mathrm{M}_\odot\,\mathrm{yr}^{-1}$)^d	$\psi(\mathrm{M}_\odot\,\mathrm{yr}^{-1})^e$
REBELS-05	6.496	$9.37^{+0.85}_{-1.0}$	44^{+15}_{-8}	$7.11^{+0.26}_{-0.29}$	18.8	$45.2^{+52.1}_{-23.5}$
REBELS-08	6.749	$9.23^{+0.64}_{-0.68}$	54^{+16}_{-10}	$7.11^{+0.19}_{-0.22}$	23.1	$112.1^{+90.9}_{-53.1}$
REBELS-12	7.349	$9.15^{+0.93}_{-0.70}$	54^{+16}_{-9}	$7.09^{+0.16}_{-0.22}$	39.0	$128.0^{+104.7}_{-59.8}$
REBELS-14	7.084	$8.94^{+0.80}_{-0.70}$	56^{+13}_{-9}	$6.87^{+0.16}_{-0.19}$	47.9	$114.2^{+38.8}_{-54.0}$
REBELS-18	7.675	$9.70^{+0.56}_{-0.73}$	39^{+12}_{-7}	$7.28^{+0.31}_{-0.31}$	34.1	$46.5^{+27.7}_{-34.1}$
REBELS-19	7.369	$9.00^{+0.69}_{-0.69}$	56^{+15}_{-10}	$6.98^{+0.13}_{-0.19}$	17.6	$126.5^{+64.0}_{-45.3}$
REBELS-25	7.306	$10.1^{+0.15}_{-0.18}$	56^{+15}_{-14}	$7.55^{+0.30}_{-0.21}$	18.8	$310.8^{+214.3}_{-115.1}$
REBELS-27	7.090	$9.90^{+0.25}_{-0.34}$	41^{+15}_{-9}	$7.13^{+0.36}_{-0.32}$	24.3	$40.7^{+46.2}_{-21.2}$
REBELS-29	6.685	$9.83^{+0.19}_{-0.19}$	42^{+16}_{-10}	$7.10^{+0.36}_{-0.32}$	34.3	$53.3^{+74.0}_{-23.8}$
REBELS-32	6.729	$9.76^{+0.35}_{-0.37}$	40^{+15}_{-9}	$7.20^{+0.34}_{-0.32}$	19.7	$31.2^{+42.6}_{-17.9}$
REBELS-38	6.577	$9.79^{+0.74}_{-1.27}$	47^{+18}_{-10}	$7.43^{+0.29}_{-0.29}$	24.8	$105.8^{+149.7}_{-47.0}$
REBELS-39	6.847	$8.77^{+0.57}_{-0.57}$	67^{+12}_{-9}	$6.82^{+0.09}_{-0.13}$	51.7	$210.5^{+9.4}_{-118.5}$
REBELS-40	7.365	$9.69^{+0.45}_{-0.99}$	44^{+17}_{-10}	$7.06^{+0.35}_{-0.31}$	21.8	$44.8^{+60.9}_{-20.0}$

Notes. [a]The stellar masses shown were derived in Stefanon et al. (in preparation) and have been re-scaled (up by 0.21 dex) so as to be consistent with a Salpeter IMF within 0.1–100 $\mathrm{M}_\odot$.
[b,c]The dust masses and temperatures have been derived as detailed in Sommovigo et al. (in preparation) using a Salpeter 0.1–100 $\mathrm{M}_\odot$ IMF.
[d]The UV SFR are the values derived in Ferrara et al. (2022) assuming a spherical dust distribution and a Milky Way extinction curve. These have been scaled up by 0.3 dex to be consistent with a Salpeter 0.1–100 $\mathrm{M}_\odot$ IMF.
[e]The total SFR is the sum of the UV and FIR SFRs where the latter is calculated as $SFR_\mathrm{IR} = L_\mathrm{IR}/10^{10}$ as detailed in Sommovigo et al. (in preparation).

presented in Sommovigo et al. (2021). The central idea of this method is to use the C II luminosity ($L_\mathrm{C\,II}$) as a proxy for the total gas mass and therefore for the dust mass, given a dust-to-gas ratio. Analytical formulas for both the dust-to-gas ratio and the C II-to-total gas conversion factors are provided in Sommovigo et al. (2021). These authors also infer the associated dust temperature and the obscured SFRs (i.e. in the FIR). The average dust temperatures for REBELS galaxies have a value of $T_\mathrm{d} \sim 49$K, as independently inferred from the calculations presented in Sommovigo et al. (in preparation) and Ferrara et al. (2022) where the latter propose an analytic method solely based on the UV and FIR continuum information. Finally, the total SFR (i.e. the sum of the FIR and UV-deduced SFRs) has been derived self-consistently with the dust temperature and mass for each galaxy in the sample using the model presented in Ferrara et al. (2022). All of these derived properties are reported in Table 2.

We now study the relation between the dust mass and stellar mass at $z \sim 7$ as shown in Fig. 2. As expected, considering SN II dust production only results in a linear relation between the dust and stellar mass such that $\log M_\mathrm{d} = \log M_* - 2.42$, i.e. a dust-to-stellar mass ratio of about 0.38 per cent. Including astration and dust destruction leaves the slope unchanged whilst leading to a decrease in the normalization (by about 0.3 dex) resulting in the dust-to-stellar mass ratio decreasing to about 0.17 per cent. Adding ejection leads to a steepening of this relation as low-mass haloes ($M_* \lesssim 10^9\mathrm{M}_\odot$) lose a larger fraction of their gas (and dust) via outflows as compared to more massive systems. As seen from this plot, adding grain growth on time-scales of $\tau_0 = 30$ Myr has only a slight effect on the relation such that for the *fiducial* model

$$\log M_\mathrm{d} = 1.15 \log M_* - 4.53, \quad (10)$$

for $M_* \sim 10^8$–$10^{11.5}\mathrm{M}_\odot$ galaxies.[6] For REBELS mass galaxies, our *fiducial* model predicts a dust-to-stellar mass ratio that increases from 0.07 to 0.1 per cent as the stellar mass increases from 10^9 to $10^{10}\mathrm{M}_\odot$.

Decreasing the grain growth time-scale to $\tau_0 = 0.3$ Myr naturally results in the dust mass rising faster with stellar mass as compared to the *fiducial* model. This is because the increase in metallicity with stellar mass leads to shorter dust accretion time-scales. However, even in this case, modulated by the gas-phase metal mass, the dust mass increases by, at most, a factor of 2 (∼0.3 dex) for REBELS mass galaxies as compared to the *fiducial model* resulting in dust-to-stellar mass ratios of about 0.16–0.24 per cent. It must be noted that even in this case, the dust masses still lie below the 'production' only model. Indeed, the upper limit is provided by the 'maximal dust mass' model wherein the dust masses are higher by about 0.8 dex for $M_* \sim 10^9$–$10^{10}\mathrm{M}_\odot$ galaxies as compared to the *fiducial* model – this model provides an upper limit to the dust-to-stellar mass ratio of about 0.63 per cent. It must be cautioned that although they cannot be excluded,[7] growth time-scales of the order of 0.3 Myr seem unlikely, if not unphysical. We end by noting that irrespective of the slope and normalization, all the theoretical models studied here predict the dust mass to scale roughly linearly with the stellar mass.

We now discuss two interesting trends in terms of the data shown in Fig. 2. First, the observationally inferred dust masses for $z \sim 7$ galaxies seem to be essentially independent of the underlying stellar mass. This somewhat flat trend is consistent with the data points

[6]Including lower mass galaxies down to $M_* \sim 10^7\mathrm{M}_\odot$ introduces a steepening of this relation such that

$$\log M_\mathrm{d} = -0.12 \log M_*^2 + 3.63 \log M_* - 16.47. \quad (11)$$

[7]Physical arguments against rapid dust growth in early galaxies are reviewed in Ferrara, Viti & Ceccarelli (2016).

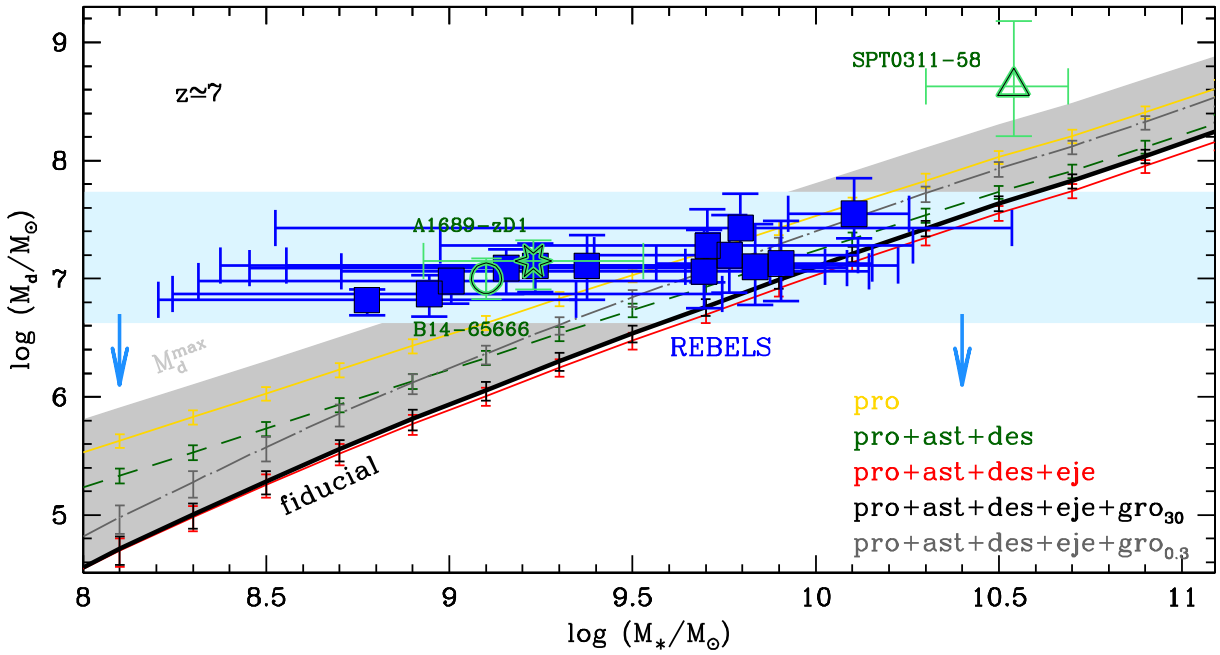

Figure 2. The dust mass as a function of stellar mass at $z \sim 7$. Solid blue points show data from REBELS (Bouwens et al. 2022; Stefanon et al. in preparation) where the stellar and dust masses have been re-scaled to a Salpeter IMF within 0.1–100 $M_\odot$. The other points show observational data for A1689−zD1 (empty star) from Watson et al. (2015) and Bakx et al. (2021), for B14−65666 (empty circle) from Hashimoto et al. (2019) and for SPT0311−58 (empty triangle) from Reuter et al. (2020). The horizontal blue shaded strip shows the dust detection limits for the REBELS program using a non-detection flux limit of 66.49 μJy (Inami et al. in preparation) assuming an average dust temperature that ranges between 30 and 80 K (these show the upper and lower limits to the dust mass, respectively). Different lines (along with 1σ error bars) show the progressive inclusion of the different dust-related physical processes discussed in Section 2.1 as in the label. The shaded grey area shows the range of dust masses demarcated by the *fiducial* model (lower limit) and the maximal dust mass model (upper limit; $M_{\rm d}^{\rm max}$).

from REBELS (Bouwens et al. 2022), using either the fiducial stellar masses from Stefanon et al. (in preparation) or those inferred by Topping et al. (in preparation), for B14−65666 (Hashimoto et al. 2019) and A1689−zD1 (Watson et al. 2015; Bakx et al. 2021) as shown in this figure; the dust mass of SPT0311−58 (Reuter et al. 2020), on the other hand, is consistent with the overall $M_{\rm d} \propto M_*$ trend predicted by our estimates.[8] We then calculate the minimum dust mass that would be detectable by the REBELS program given its non-detection dust continuum flux limit of about 66.49 μJy. We find this minimum dust mass to have a value of about $10^{7.7}$ ($10^{6.6}$)$M_\odot$ assuming a dust temperature of 30 K (80 K). This naturally biases our observations to only detecting galaxies with higher dust masses, especially for $M_* \lesssim 10^{9.5}$ ($10^{8.8}$)$M_\odot$ systems as per the *fiducial* (*maximal* dust model, even assuming dust temperatures as high as 80 K. The flatness of this relation can therefore be attributed to an observational bias introduced by the continuum detection limit of the REBELS program.

Secondly, and more crucially, within error bars the bulk of the REBELS observations are consistent with our *fiducial* model as seen from this figure. However, two of the lowest mass galaxies (REBELS-19 and 39), with $8.7 < \log(M_*/M_\odot) < 9$, are clear outliers. These show dust masses and dust-to-stellar mass ratios ($\sim$ 0.94–1.1 per cent) that are up to 18× higher for a given stellar mass as compared to the *fiducial* model (see also Table 2); REBELS-14 is the third of the lowest-mass galaxies (reference stellar mass of $10^{8.73}M_\odot$) that is only consistent with the *fiducial* model if its stellar mass lies at the observationally inferred upper limit of $M_* \sim 10^{9.7}M_\odot$. Matching REBELS-19 and 39 within error bars requires scenarios that lie between the 'no dust ejection' and 'maximal dust mass' models; the lowest-mass galaxy (REBELS-39) has a dust mass that lies between the 'production only' and 'maximal dust mass' models, even if its stellar mass is assumed to be at the upper limit predicted by observations; the above results remain qualitatively unchanged even if the higher stellar masses inferred by Topping et al. (in preparation) are used. Indeed, even ignoring any dust loss in astration, destruction, and ejection, explaining the dust masses of these systems would require each SN II to produce $\sim$ 1.25–1.5$M_\odot$ of dust (after SN shock processing; assuming a Salpeter 0.1–100 $M_\odot$ IMF) that is higher than any observational estimate so far; using the stellar masses from Topping et al. (in preparation) would require each SN II to produce lower dust masses of $\sim$ 0.57–0.74$M_\odot$, bringing them into agreement with observed SN dust yields (ranging within 0.03–1.1$M_\odot$). Finally, we note that within error bars, the 'maximal dust mass' model also encompasses the dust masses inferred for A1689−zD1 (Watson et al. 2015; Bakx et al. 2021), B14−65666 (Hashimoto et al. 2019), and SPT0311-58 (Reuter et al. 2020).

We can also compute an upper limit to the dust mass from both production and grain growth for a galaxy of $M_* \sim 10^9M_\odot$: assuming each SN II to produce 1$M_\odot$ of dust would yield $\sim 10^{6.9}M_\odot$ of dust using our chosen IMF. Further assuming all the gas-phase metals ($M_Z \sim 10^{6.4}M_\odot$) to have condensed into dust (i.e. resulting in a $M_Z = 0$) would yield a total dust mass of $M_{\rm d} \sim 10^7M_\odot$. This yields a dust-to-stellar mass ratio of 1 per cent, assuming all the metals to have condensed into dust that is still below the inferred values

[8]However, we caution this source is composed of two individual galaxies at $z = 6.9$, which are lensed by different amounts, complicating the picture.

for some of the observed sources (namely REBELS-19 and 39) and very close to the values inferred for A1689−zD1 and B14−65666. Alternatively, either (i) the dust mass deduced from the data could be overestimated, for example, if the assumed temperature is too low as suggested by a number of theoretical works (e.g. Behrens et al. 2018; Liang et al. 2019; Sommovigo et al. 2020), or, more possibly, (ii) the stellar mass could be underestimated for these low-mass galaxies. Indeed, employing non-parametric SFHs, Topping et al. (in preparation) find the stellar masses of the lowest-mass galaxies ($M_* \lesssim 10^{9.2}$M$_\odot$) to be higher by a factor of 3–10. We compare our dust-to-stellar mass relation with those from a number of other semi-analytic models (e.g. Popping et al. 2017; Vijayan et al. 2019; Triani et al. 2020) in Appendix A.

We then show the dust-to-gas-ratio ($\mathcal{D}$) as a function of the stellar mass in (the left-hand panel of) Fig. 3. As expected, this value is the highest for the production only model with $\mathcal{D} \sim 15$ per cent for low-mass ($M_* \sim 10^{7.2}$M$_\odot$) galaxies, given their low gas contents. For $M_* \gtrsim 10^9$M$_\odot$ galaxies that are massive enough to retain most of their gas mass, the stellar (and dust) mass effectively scale with the gas mass resulting in $\mathcal{D}$ saturating at ~ 0.27 per cent. Including astration and destruction leads to a decrease in the dust-to-gas ratio by about 0.3 dex at $M_* \gtrsim 10^{8.5}$M$_\odot$ resulting in $\mathcal{D} \sim 0.14$ per cent. Preferentially decreasing the dust and gas mass contents of low-mass ($M_* \lesssim 10^{7.5}$M$_\odot$) galaxies, including ejection completely changes the mass dependence of $\mathcal{D}$ by decreasing it by about 2.5 orders of magnitude at this low-mass end. At the high-mass ($M_* \gtrsim 10^9$M$_\odot$) end, ejection only decreases the amplitude of the dust-to-gas ratio by about 0.15 dex resulting in $\mathcal{D} \sim 0.1$ per cent. Including grain growth on a time-scale of $\tau_0 = 30$Myr (*fiducial* model) has no appreciable impact on this relation. Similarly, including grain growth on a $\tau_0 = 0.3$-Myr time-scale leads to only a small increase in $\mathcal{D}$ by about 0.3 dex compared to the fiducial model – in this case, the value of $\mathcal{D}$ increases with stellar mass, reaching $\mathcal{D} \sim 0.2$ per cent for $M_* \sim 10^9$–10^{10}M$_\odot$ galaxies. However, we reiterate that even in this case, the 'production only' model provides the upper limit to the dust-to-gas ratio. As shown in the same panel, in the *fiducial* model the metallicity for these galaxies increases from about 12 to 26 per cent of the solar value as the stellar mass increases from $10^{7.5}$ to $10^{11.5}$M$_\odot$. As expected, a larger amount of metals saturate into dust assuming $\tau_0 = 0.3$Myr. This naturally results in a decrease in the metallicity values for all masses: in this case, the metallicity increases from 9 to 18 per cent for $M_* \sim 10^{7.5}$–$10^{11.5}$M$_\odot$ galaxies. Finally, for the *fiducial* model, we find a relation

$$\log(\mathcal{D}) = 1.02 \log(Z/Z_\odot) - 2.33. \quad (12)$$

This linear relation between the dust-to-gas ratio and the gas-phase metallicity is in accordance with a number of previous observational and theoretical results (e.g. Draine & Li 2007; Leroy et al. 2011; Rémy-Ruyer et al. 2013; Hou et al. 2019; Li et al. 2019)

We then study the dust-to-metal ratio as a function of stellar mass (right-hand panel of Fig. 3). At $z \sim 7$, the dust-to-metal ratio has a constant value (~ 37 per cent) in the production only scenario. Including astration and destruction naturally decreases this value, to $M_d/M_Z \sim 26$ per cent. Further including the process of ejection results an increase (of about 0.1 dex) in the dust-to-metal ratio for $M_* \lesssim 10^8$M$_\odot$ haloes whilst leaving the value largely unchanged at larger masses. This increase occurs because assuming perfect mixing (of metals and dust with gas) results in a larger amount of metals being ejected as compared to dust. Whilst including dust growth on a $\tau_0 = 30$-Myr time-scale hardly affects this ratio for low-mass galaxies ($M_* \lesssim 10^{7.6}$M$_\odot$), given their low metallicities, the dust-to-metal ratio increases with stellar mass for more massive haloes; e.g. for $M_* \sim 10^{10}$M$_\odot$ galaxies, the value of $M_d/M_Z \sim 34$ per cent. Finally, including grain growth on a $\tau_0 = 0.3$-Myr time-scale leads to a steeper increase in the M_d/M_Z value - for REBELS-type galaxies ($M_* \sim 10^9$–10^{10}M$_\odot$), $M_d/M_Z \sim 1$ is a factor of 2.7 higher in this model compared to the *fiducial* model.

4 DUST OBSCURATION EFFECTS

We now discuss the observational implications of the presence of the predicted amount of dust in early galaxies, specially on their UV LF (Section 4.1) and the UV-to-total SFR relation (Section 4.2).

4.1 The impact of dust obscuration on the UV LF

As dust can heavily obscure UV radiation it is natural to base the analysis on the $z \sim 7$ UV LF, as shown in Fig. 4. As seen, the theoretical *intrinsic* (i.e. unattenuated) UV LF starts overpredicting the number of bright galaxies with respect to observations at an absolute magnitude $M_{UV} \lesssim -21.2$. This implies that in these systems, some dust attenuation is required, with the dust continuum FIR emission observed by REBELS confirming this hypothesis.

However, only including SN II dust production results in a theoretical UV LF that is both lower in amplitude and steeper than the observed one in our model, cutting off at $M_{UV} \sim -21.9$. The dust attenuation naturally decreases when the effect of astration and destruction are taken into account. As seen from the same figure, these two processes alone are almost sufficient to bring the UV LF into broad agreement with observations. Including ejection further increases the amplitude of the UV LF, that however, remains virtually unchanged once grain growth on a $\tau_0 = 30$ Myr is included. Thus, our *fiducial* model fits the observed UV LF at $z \sim 7$ for $M_{UV} \sim -18$ to -23 extremely well. Assuming grain growth on a $\tau_0 = 0.3$ Myr time-scale results in the model UV LF underpredicting the observations at $M_{UV} \lesssim -21.4$, showing a cut-off at $M_{UV} \sim -22.1$. Finally, the 'maximal dust mass' model provides the lower limit to the UV LF, underpredicting the data for $M_{UV} \lesssim -19.2$ and showing a complete cut-off at $M_{UV} \sim -21$.

The large dust masses observationally inferred for $M_* \lesssim 10^{9.5}$M$_\odot$ galaxies at $z \sim 7$ are therefore incompatible with the UV LF. This discrepancy could be reconciled if (i) such low-mass highly dusty galaxies are outliers that are not representative of the 'average' LBG population making up the UV LF; or (ii) not all of the dust mass contributes to UV attenuation. This second effect could be explained by a *spatial segregation* between dust and star-forming regions (Inami et al., in preparation; Ferrara et al. 2022) as has been found both in theoretical models (Mancini et al. 2016; Behrens et al. 2018; Cochrane et al. 2019; Liang et al. 2019; Sommovigo et al. 2020) and observations (Hodge et al. 2016; Carniani et al. 2017; Laporte et al. 2017; Hashimoto et al. 2019) or most of the dust is diffused into the ISM with only a small fraction (~ 15 per cent) attenuating the UV light from star forming regions; or (iii) the stellar masses have been underestimated for these low-mass systems (see discussion in Topping et al. in preparation); or (iv) the dust temperatures have been underestimated for low-mass systems, leading to an overestimation of their dust content.

In any case, the UV LF provides valuable indication that the processes of production, astration, destruction and ejection are key in shaping the dust content, with grain growth only playing a minor role.

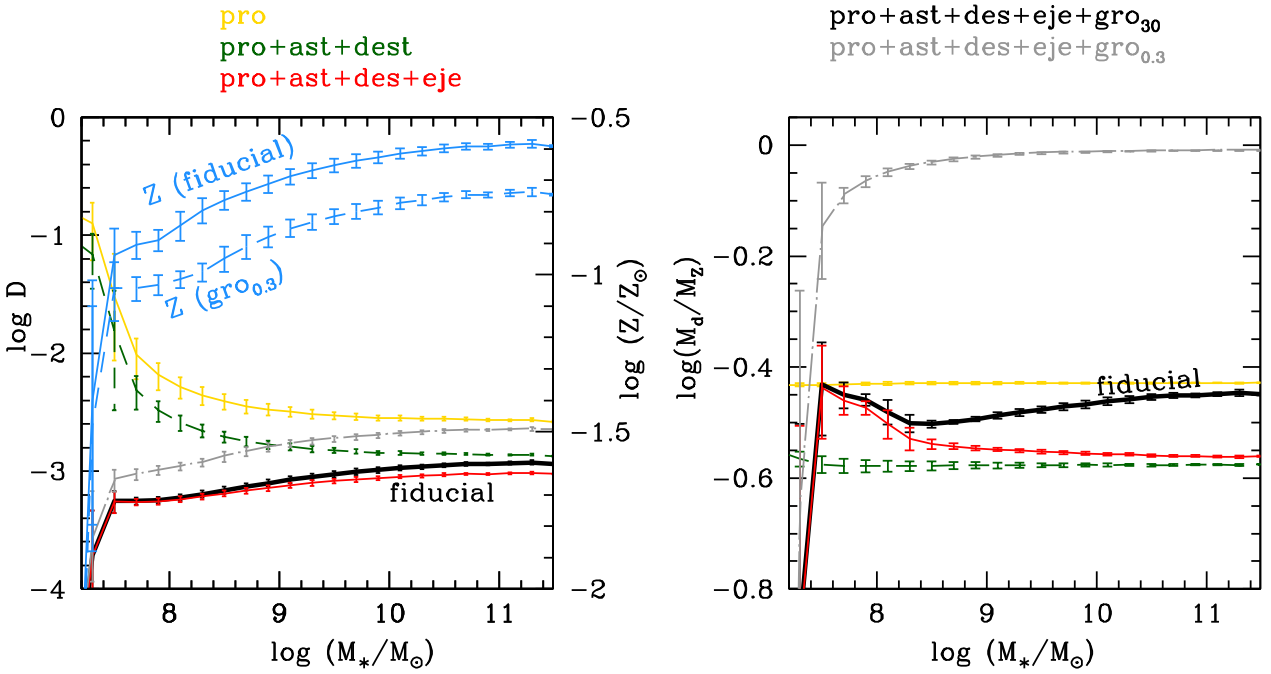

Figure 3. As a function of the stellar mass at $z \sim 7$, for the different dust-related physical processes discussed in Section 2.1 and described in the label, we show the dust-to-gas ratio ($\mathcal{D}$) and the metallicity normalized to solar units (blue lines) in the left-hand panel and the dust-to-metal mass ratio (M_d/M_Z) in the right-hand panel.

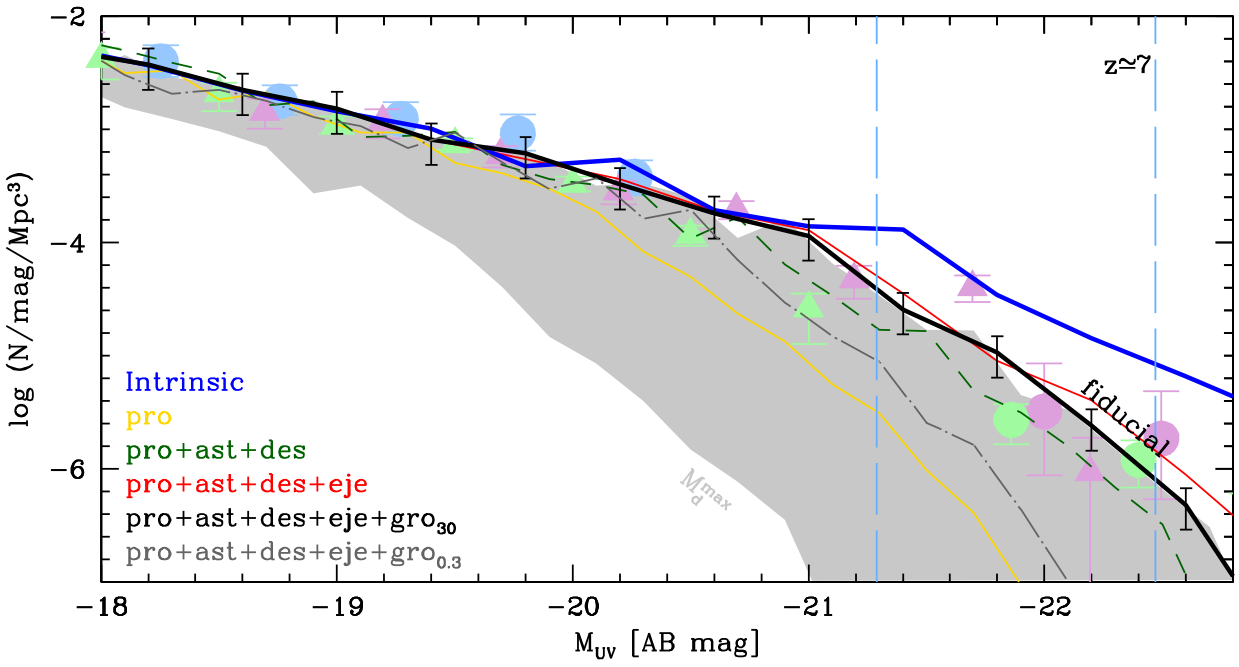

Figure 4. The UV LF at $z \sim 7$. Points show observational data collected by different groups: McLure et al. (2013, green triangles), Atek et al. (2015, blue circles), Bowler et al. (2017, green circles), Harikane et al. (2022, violet circles), and Bouwens et al. (2021, violet triangles). The lines show the average UV LF for the dust processes noted, with the solid blue line showing the *intrinsic* UV LF. The shaded grey area shows the UV LF range demarcated by the *fiducial* model (upper limit) and the maximal dust mass model (lower limit; M_d^{max}). Finally, the dashed vertical lines show the range of UV magnitudes ($M_{UV} \sim -22.47$ to -21.29) observed for REBELS sources.

4.2 The impact of dust obscuration on the UV-to-total SFR relation

Finally, we discuss the relation between the SFR inferred from the UV luminosity of a galaxy (ψ_{UV}), and the total intrinsic SFR ($=\psi$) in Fig. 5. As might be expected from the above discussions, for a given value of ψ, the value of ψ_{UV} progressively increases as the processes of dust astration, destruction and ejection are added to the 'dust production' only model. Including ISM grain growth on a 30-

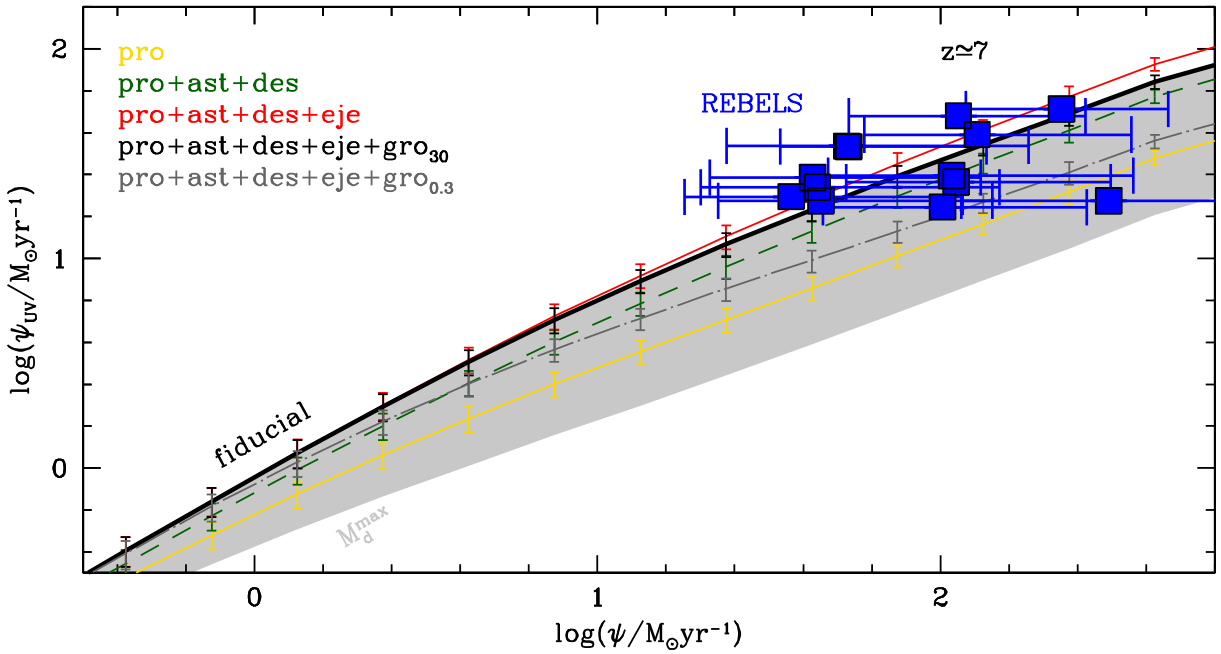

Figure 5. The UV SFR ($\psi_{\rm UV}$) as a function of the total SFR (ψ) at $z \sim 7$. Filled squares show SFRs from the REBELS data (Ferrara et al. 2022) re-scaled using a Salpeter IMF within 0.1–100 $M_\odot$; lines are the predicted average values (along with 1σ error bars) considering the different dust processes modelled, as noted. Finally, the shaded grey area shows the range of SFR_{UV} demarcated by the *fiducial* model (upper limit) and the maximal dust mass model (lower limit; $M_{\rm d}^{\rm max}$).

Myr time-scale naturally decreases $\psi_{\rm UV}$ slightly (by about 0.1 dex) with this *fiducial* model predicting a quadratic relation such that

$$\log(\psi_{\rm UV}) = -0.05\,[\log(\psi)]^2 + 0.86\log(\psi) - 0.05. \quad (13)$$

This relation is valid for SFRs ranging over five orders of magnitude, within $\sim 10^{-2.5}$–10^3 $M_\odot yr^{-1}$. For REBELS-type galaxies, with $\psi \sim$ 30–310 $M_\odot yr^{-1}$, our *fiducial* model predicts $\psi_{\rm UV} \sim$ 10–50 $M_\odot yr^{-1}$. While, within error bars, the bulk of the REBELS galaxies lie close to the fiducial model, there are a number of outliers (namely REBELS-19 and 25) that show $\psi_{\rm UV}$ values that a factor of 2–3 times smaller for a given ψ value. These galaxies are more dust attenuated as compared to our *fiducial* model predictions, which is in accord with the (up to 18 times) higher dust masses shown by some of the REBELS galaxies (specially REBELS-19) when compared to the *fiducial* model as detailed in Section 3.

Compared to the *fiducial* model, the slightly higher dust masses (by a factor of ∼2) in the model with $\tau_0 = 0.3$ Myr result in a corresponding decrease in the UV SFR (that range within 8–30 $M_\odot yr^{-1}$). The results for this model therefore lie between the *fiducial* and the 'production only' models. Finally, the 'maximal dust mass' model provides a lower limit to the $\psi_{\rm UV}$ for a given value of the total SFR. For REBELS galaxies, this model predicts $\psi_{\rm UV}$ values $\sim$ 5–13 $M_\odot$ yr^{-1} that are a factor of 2–4 lower than those predicted by the *fiducial* model. We reiterate that with its extremely high extinction of UV light, the 'maximal dust mass' model is incompatible with the observed $z \sim 7$ UV LF.

We now discuss the trend of $f_{\rm c}$ as a function of the total SFR and the stellar mass, as shown in Fig. 6. We remind the reader that we have defined $f_{\rm c} = \psi_{\rm UV}/\psi$. Starting with the 'production only' model, $f_{\rm c}$ decreases by about an order of magnitude (from ∼0.75 to 0.075) as the total SFR increases from $\psi \sim 0.3$ to 630 $M_\odot$ yr^{-1} reflecting the increasing impact of dust attenuation in increasingly massive systems. Further, $\psi_{\rm UV} > 0.5$ only for galaxies with $\psi \lesssim 2.4\,M_\odot$ yr^{-1} i.e. galaxies with higher total SFRs will be increasingly suppressed in terms of their UV luminosity. The value of $f_{\rm c}$ naturally increases when the processes of dust astration, destruction, and ejection are added. Including these effects, the UV SFR dominates in galaxies with SFRs as high as $\psi \sim 35$ $M_\odot$ yr^{-1}. These results change only slightly for the *fiducial* model where $f_{\rm c} \sim 0.5$ for a slightly smaller value of $\psi \sim 25$ $M_\odot$ yr^{-1}. The model with grain growth on a 0.3-Myr time-scale yields the steepest decrease of $f_{\rm c}$ with ψ as a result of the increase in dust mass in such massive systems. Finally, the 'maximal dust mass' model yields the lower limit to the unobscured SFR: In this model, $\psi_{\rm UV} \sim 0.5$, i.e. the UV SFR is obscured, for a total SFR value as low as 0.6 $M_\odot$ yr^{-1}

We also see that the trend of $f_{\rm c}$ shallows with increasing halo mass for all models – this is driven by the fact that the virial radius increases faster than the dust mass. For REBELS galaxies, $f_{\rm c}$ only decreases by a factor of 2.25 from ∼ 45 to ∼ 20 per cent as ψ increases by about an order of magnitude from ∼40 to ∼ 300$M_\odot$ yr^{-1}, as seen in Fig. 6. The *fiducial* model therefore predicts that 55 per cent (80 per cent) of the SFR in the UV is obscured for galaxies with $\psi \sim 40\,(300) M_\odot$ yr^{-1}, which has enormous implications for the SFRD at such high-z. This is in accordance with the results of Ferrara et al. (2022) who have independently derived attenuation values ranging between 28 and 91 per cent for the same galaxies based on their UV spectral slopes.

With respect to comparison with observations, we limit these to results from the REBELS survey, whilst noting that similar results have been found at lower redshifts ($z \sim$ 4.4–5.8) for about 118 galaxies in the rest frame at 158 μm as part of the Atacama Large Millimeter Array Large Program to INvestigate [C II] at Early times (ALPINE) survey (Fudamoto et al. 2020). As seen, our results are in excellent agreement with the overall trend of $f_{\rm c}$ decreasing with ψ shown by the REBELS data. Furthermore, the bulk of these data points either lie on the *fiducial* model, or are consistent with it within error bars. The only two outliers in this case are also REBELS-19 and 25 as might be expected from the discussion above.

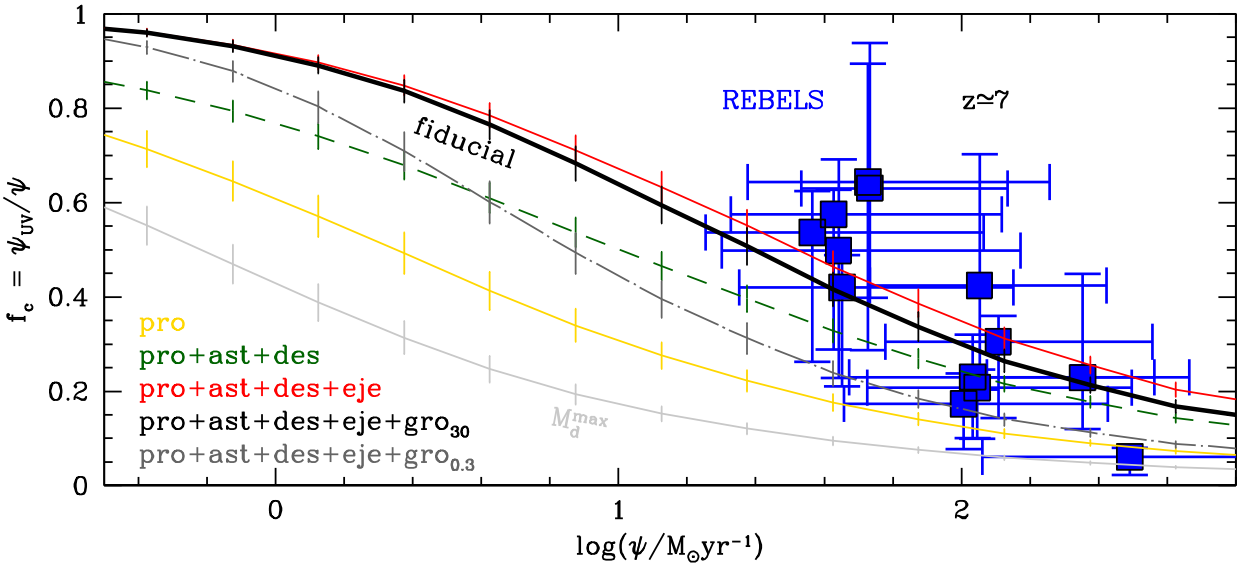

Figure 6. The UV escape fraction ($f_c = \psi_{UV}/\psi$) as a function of the total SFR for $z \sim 7$ galaxies. The different lines show the predicted average values (along with 1σ error bars) considering the different dust processes modelled, as noted. The filled squares show the data from the REBELS program where the SFRs have been calculated as described in Ferrara et al. (2022) and re-scaled for a Salpeter IMF between 0.1 and 100$M_\odot$.

5 CONCLUSIONS AND DISCUSSION

In this work, we have included a fully coupled treatment of metal and dust enrichment into the DELPHI semi-analytic model of galaxy formation. Our aim is to study the relative importance of the various processes (production, astration, destruction, ejection, and ISM grain growth) regulating the dust content of high-redshift LBGs. In addition to studying dust masses using two different ISM grain growth time-scales, $\tau_0 = 30$ (*fiducial* model) and 0.3 Myr, we explore a (clearly unphysical) 'maximal dust mass' model to provide an upper limit to the dust enrichment of such early galaxies. Our key findings at $z \sim 7$ are as follows:

(i) In the *fiducial* model, dust production governs the dust content of $M_* \sim 10^9$–$10^{10}M_\odot$ galaxies over their entire lifetime; by $z \sim 7$. On average, for such galaxies, astration + destruction and ejection are each ~ 40 per cent (~ 60 per cent) as important as production for the *fiducial* ($\tau_0 = 0.3$ Myr) model.

(ii) For the *fiducial* model, the dust and stellar mass are related as $M_d = 1.15 \log M_* - 4.53$. Predicting dust-to-stellar mass ratios ~ 0.07–0.1 per cent, this relation is in good agreement with the majority of the REBELS-detected points except for two sources (REBELS-19 and 39); these show dust-to-stellar mass ratios that are up to a factor 18 higher than the *fiducial* model - this result holds independently of the stellar masses inferred for REBELS galaxies (e.g. by Stefanon et al. in preparation; Topping et al. in preparation) that, on average, differ by 0.55 dex, depending on the SFH used. Crucially, due to the physical coupling between dust and metal enrichment, even decreasing τ_0 to 0.3 Myr only increases the dust-to-stellar mass ratio by a factor < 2. Hence, grain growth cannot be advocated to explain extremely high ratios.

(iii) In the *fiducial* model the dust-to-gas ratio is $\mathcal{D} \sim 0.1$ per cent for $M_* \sim 10^9$–$10^{10}M_\odot$ REBELS-mass galaxies; for $\tau_0 = 0.3$ Myr, it only increases by a factor of ≈ 2, i.e. $\mathcal{D} \sim 0.2$ per cent.

(iv) The dust-to-metal mass ratio has a value $M_d/M_Z \sim 0.34$ in the *fiducial* model. This increases to $M_d/M_Z \sim 1$ for the model with $\tau_0 = 0.3$ Myr i.e. the total amount of metals produced by stars is equally split between the gas and the solid (grain) phase.

(v) Models not including dust attenuation largely overpredict the UV LF at $M_{UV} \lesssim -21.2$ (see e.g. Bouwens et al. 2009; Reddy et al. 2010). The *fiducial* model yields instead results in excellent agreement with observations, and in close agreement with a model without any grain growth. However, grain growth with a 0.3-Myr time-scale underpredicts the UV LF at all $M_{UV} \lesssim -21.4$.

(vi) The *fiducial* model predicts the UV SFR (ψ_{UV}) and total SFR (ψ) to be related as $\log(\psi_{UV}) = -0.05\,[\log(\psi)]^2 + 0.86 \log(\psi) - 0.05$ for $\psi \sim 10^{-2.6}$–10^3 $M_\odot yr^{-1}$.

(vii) The *fiducial* model predicts a UV escape fraction ranging between 20 and 45 per cent for REBELS galaxies, i.e. 55 per cent (80 per cent) of the SFR in the UV is obscured for galaxies with $\psi \sim 40\,(300) M_\odot$ yr^{-1}. With its larger dust masses, the model with $\tau_0 = 0.3$ Myr naturally predicts a larger attenuation fraction of 70 per cent (90 per cent) over the same SFR range.

While the bulk of the REBELS observations are consistent with our *fiducial* model, there are two low-mass outliers (REBELS-19, 39) with $8.7 < \log(M_*/M_\odot) < 9.0$ that show dust-to-stellar mass values that are up to a factor of 18 higher. This somewhat flat trend is also consistent with other data points for low-mass $z \sim 7$ galaxies (Watson et al. 2015; Hashimoto et al. 2019). Within error bars, our unphysical 'maximal dust mass' model (that only includes production assuming a dust yield of $1M_\odot$ per SN II, astration, and grain growth on a $\tau_0 =$ 0.3-Myr time-scale) can reproduce the dust masses for the REBELS galaxies as well as for the other $z \sim 7$ dusty galaxies including A1689−zD1 (Watson et al. 2015; Bakx et al. 2021), B14−65666 (Hashimoto et al. 2019), and SPT0311−58 (Reuter et al. 2020). However, such high dust masses result in an underprediction of the UV LF for $M_{UV} \gtrsim -19.5$.

This tension can be resolved by four different possibilities: (i) such low-mass, highly dusty galaxies are outliers that are not representative of the 'average' LBG population making up the UV LF; (ii) not all of the dust mass observed contributes to UV attenuation either because dust and star forming regions are *spatially segregated* or a large fraction of dust is diffused into the ISM with only a small fraction contributing to attenuating UV light; (iii) the dust masses for these low-mass systems are overestimated due to an

underestimation in the dust temperature; and (iv) the stellar masses have been underestimated, especially for the lowest mass systems observed by REBELS. Explanation (ii) is particularly relevant for REBELS-39 that shows a UV-to-total SFR relation in agreement with the *fiducial* model whilst having a dust mass that lies above this relation. REBELS-25 is an outlier that shows a larger attenuation of its UV SFR despite its dust mass being in perfect agreement with the *fiducial* relation. This might hint at dust being *preferentially clumped* around sites of young star formation.

Finally, we end with a few caveats of the model. First, we have assumed gas, metals and dust to be perfectly mixed in the ISM. Along the same lines, secondly, we have assumed a dust radius that is equal to the gas radius, and a homogeneous slab-like dust distribution within this. In principle, one might expect dust to be more concentrated in newly star-forming regions and more dispersed into the ISM for older populations. Thirdly, we have ignored AGB contribution to the dust values inferred. However, as noted, this is expected to affect the inferred dust masses only slightly, i.e. at the $\sim$ 10 per cent level. Fourthly, we have neglected local overdensities of cold gas that might increase the ISM grain growth rate. Finally, we assume smoothly-accreted gas to be devoid of both metals and dust. This might be an underestimation in the case of 'galactic fountains', i.e. when a part of the metal/dust-enriched gas ejected in at an earlier time is re-accreted on to the galaxy at a later stage. This is an effect that is already being included into our semi-numerical grid-based ASTRAEUS (Hutter et al. 2021) framework. Over the next years, a growing amount of ALMA data will be crucial in shedding light on a number of these outstanding issues. This includes properly sampled dust SEDs to address the dust temperature and the impact of the cosmic microwave background, matched-resolution ALMA/*JWST* (*James Webb Space Telescope*) imaging to directly address the patchy obscuration issue, adding more 'direct' ISM tracers than [C II] and higher spatial resolution observations to understand the UV and dust distributions (planned as part of the CRISTAL ALMA large program; PI: Herrera-Camus).

ACKNOWLEDGEMENTS

PD and JB acknowledge support from the European Research Council's starting grant ERC StG-717001 ('DELPHI'). PD also acknowledges support from the NWO grant 016.VIDI.189.162 ('ODIN') and the European Commission's and University of Groningen's CO-FUND Rosalind Franklin program and thanks Maxime Trebitsch for interesting discussions. AF and AP acknowledge support from the ERC Advanced Grant INTERSTELLAR H2020/740120. Any dissemination of results must indicate that it reflects only the author's view and that the Commission is not responsible for any use that may be made of the information it contains; partial support from the Carl Friedrich von Siemens-Forschungspreis der Alexander von Humboldt-Stiftung Research Award is kindly acknowledged. RJB and MS acknowledge support from TOP grant TOP1.16.057. RS acknowledges support from an STFC Ernest Rutherford Fellowship (ST/S004831/1). SS acknowledges support from the Nederlandse Onderzoekschool voor Astronomie (NOVA). CK acknowledges funding from the UK STFC through grants ST/ R000905/1 and ST/V000632/1. MA acknowledges support from FONDECYT grant 1211951, 'ANID+PCI+INSTITUTO MAX PLANCK DE ASTRONOMIA MPG 190030', 'ANID+PCI + REDES 190194', and ANID BASAL project FB210003. EdC gratefully acknowledges support from the Australian Research Council Centre of Excellence for All Sky Astrophysics in 3 Dimensions (ASTRO 3D), through project number CE170100013. YF acknowledges support from NAOJ ALMA Scientific Research Grant number 2020-16B. JH gratefully acknowledges support of the VIDI research program with project number 639.042.611, which is (partly) financed by the Netherlands Organisation for Scientific Research (NWO). HI and HSBA acknowledge support from the NAOJ ALMA Scientific Research Grant Code 2021-19A. HI acknowledges support from the JSPS KAKENHI Grant Number JP19K23462. IDL acknowledges support from ERC starting grant DustOrigin 851622. RE acknowledges funding from *JWST*/NIRCam contract to the University of Arizona, NAS5-02015. This paper is based on data obtained with the ALMA Observatory, under the Large Program 2019.1.01634.L. ALMA is a partnership of ESO (representing its member states), NSF (USA), and NINS (Japan), together with NRC (Canada), MOST and ASIAA (Taiwan), and KASI (Republic of Korea), in cooperation with the Republic of Chile. The Joint ALMA Observatory is operated by ESO, AUI/NRAO, and NAOJ.

DATA AVAILABILITY

Data generated in this research will be shared on reasonable request to the corresponding author.

REFERENCES

Aoyama S., Hou K.-C., Shimizu I., Hirashita H., Todoroki K., Choi J.-H., Nagamine K., 2017, MNRAS, 466, 105
Asplund M., Grevesse N., Sauval A. J., 2005, in Barnes T. G. III, Bash F. N., eds, ASP Conf. Ser. Vol. 336, Cosmic Abundances as Records of Stellar Evolution and Nucleosynthesis. Astron. Soc. Pac., San Francisco, p. 25
Atek H. et al., 2015, ApJ, 814, 69
Bakx T. J. L. C. et al., 2020, MNRAS, 493, 4294
Bakx T. J. L. C. et al., 2021, MNRAS, 508, L58
Behrens C., Pallottini A., Ferrara A., Gallerani S., Vallini L., 2018, MNRAS, 477, 552
Bekki K., 2015, MNRAS, 449, 1625
Bianchi S., Schneider R., 2007, MNRAS, 378, 973
Bocchio M., Marassi S., Schneider R., Bianchi S., Limongi M., Chieffi A., 2016, A&A, 587, A157
Bouwens R. J. et al., 2009, ApJ, 705, 936
Bouwens R. J. et al., 2021, AJ, 162, 47
Bouwens R. J. et al., 2022, ApJ, preprint (arXiv:2106.13719)
Bouwens R., Aravena M., Decarli R. et. al., 2016, ApJ, 833, 72
Bowler R. A. A., Dunlop J. S., McLure R. J., McLeod D. J., 2017, MNRAS, 466, 3612
Calvi V. et al., 2016, ApJ, 817, 120
Calzetti D., Armus L., Bohlin R. C., Kinney A. L., Koornneef J., Storchi-Bergmann T., 2000, ApJ, 533, 682
Carniani S. et al., 2017, A&A, 605, A42
Castellano M., Fontana A., Paris D. et. al., 2010, A&A, 524, A28
Chabrier G., 2003, ApJ, 586, L133
Chevallard J., Charlot S., 2016, MNRAS, 462, 1415
Cochrane R. K. et al., 2019, MNRAS, 488, 1779
Davis A. J., Natarajan P., 2009, MNRAS, 393, 1498
Dayal P., Ferrara A., 2018, Phys. Rep., 780, 1
Dayal P., Ferrara A., Dunlop J. S., Pacucci F., 2014, MNRAS, 445, 2545
Dayal P., Ferrara A., Saro A., 2010, MNRAS, 402, 1449
de Bennassuti M., Schneider R., Valiante R., Salvadori S., 2014, MNRAS, 445, 3039
Draine B. T., 2003, ARA&A, 41, 241
Draine B. T., Li A., 2007, ApJ, 657, 810
Duncan K. et al., 2014, MNRAS, 444, 2960
Dunlop J. S. et al., 2013, MNRAS, 432, 3520
Dwek E., 1998, ApJ, 501, 643
Faisst A. L., Fudamoto Y., Oesch P. A., Scoville N., Riechers D. A., Pavesi R., Capak P., 2020, MNRAS, 498, 4192

Ferrara A. et al., 2022, MNRAS, 512, 58
Ferrara A., 2016, Astrophysics and Space Science Library, Vol. 423, Understanding the Epoch of Cosmic Reionization: Challenges and Progress. Springer, Berlin, p. 163
Ferrara A., Pettini M., Shchekinov Y., 2000, MNRAS, 319, 539
Ferrara A., Viti S., Ceccarelli C., 2016, MNRAS, 463, L112
Finkelstein S. L. et al., 2015, ApJ, 810, 71
Fudamoto Y. et al., 2020, A&A, 643, A4
Fudamoto Y. et al., 2021, Nature, 597, 489
González V., Labbé I., Bouwens R. J., Illingworth G., Franx M., Kriek M., 2011, ApJ, 735, L34
Graziani L., Schneider R., Ginolfi M., Hunt L. K., Maio U., Glatzle M., Ciardi B., 2020, MNRAS, 494, 1071
Gutkin J., Charlot S., Bruzual G., 2016, MNRAS, 462, 1757
Harikane Y. et al., 2022, ApJS, 259, 20
Hashimoto T. et al., 2019, PASJ, 71, 71
Hodge J. A. et al., 2016, ApJ, 833, 103
Hodge J. A., da Cunha E., 2020, R. Soc. Open Sci., 7, 200556
Hou K.-C., Aoyama S., Hirashita H., Nagamine K., Shimizu I., 2019, MNRAS, 485, 1727
Hutter A., Dayal P., Yepes G., Gottlöber S., Legrand L., Ucci G., 2021, MNRAS, 503, 3698
Ishigaki M., Kawamata R., Ouchi M., Oguri M., Shimasaku K., Ono Y., 2018, ApJ, 854, 73
Kannan R., Garaldi E., Smith A., Pakmor R., Springel V., Vogelsberger M., Hernquist L., 2021, MNRAS, 3, 4005
Kobayashi C., Karakas A. I., Lugaro M., 2020, ApJ, 900, 179
Laporte N. et al., 2017, ApJ, 837, L21
Leitherer C. et al., 1999, ApJS, 123, 3
Leroy A. K. et al., 2011, ApJ, 737, 12
Leśniewska A., Michałowski M. J., 2019, A&A, 624, L13
Li Q., Narayanan D., Davé R., 2019, MNRAS, 490, 1425
Liang L. et al., 2019, MNRAS, 489, 1397
Lisenfeld U., Ferrara A., 1998, ApJ, 496, 145
Livermore R. C., Finkelstein S. L., Lotz J. M., 2017, ApJ, 835, 113
Mancini M., Schneider R., Graziani L., Valiante R., Dayal P., Maio U., Ciardi B., 2016, MNRAS, 462, 3130
Mancini M., Schneider R., Graziani L., Valiante R., Dayal P., Maio U., Ciardi B., Hunt L. K., 2015, MNRAS, 451, L70
Marrone D. P. et al., 2018, Nature, 553, 51
Matsuura M. et al., 2015, ApJ, 800, 50
McKee C. F., 1989, ApJ, 345, 782
McKinnon R., Vogelsberger M., Torrey P., Marinacci F., Kannan R., 2018, MNRAS, 478, 2851
McLure R. J. et al., 2013, MNRAS, 432, 2696
Michałowski M. J., 2015, A&A, 577, A80
Niculescu-Duvaz M., Barlow M. J., Bevan A., Milisavljevic D., De Looze I., 2021, MNRAS, 504, 2133
Nozawa T., Kozasa T., Umeda H., Maeda K., Nomoto K., 2003, ApJ, 598, 785
Oesch P. A., Bouwens R. J., Illingworth G. D., Labbé I., Stefanon M., 2018, ApJ, 855, 105
Oke J. B., Gunn J. E., 1983, ApJ, 266, 713
Padovani P., Matteucci F., 1993, ApJ, 416, 26
Pallottini A. et al., 2019, MNRAS, 487, 1689
Planck CollaborationXLVII, 2016, A&A, 596, A107
Popping G., Somerville R. S., Galametz M., 2017, MNRAS, 471, 3152
Priestley F. D., Barlow M. J., De Looze I., Chawner H., 2020, MNRAS, 491, 6020
Reddy N. A., Erb D. K., Pettini M., Steidel C. C., Shapley A. E., 2010, ApJ, 712, 1070
Rémy-Ruyer A. et al., 2013, A&A, 557, A95
Reuter C. et al., 2020, ApJ, 902, 78
Rho J. et al., 2018, MNRAS, 479, 5101
Salpeter E. E., 1955, ApJ, 121, 161
Schouws S. et al., 2021, ApJ, preprint (arXiv:2105.12133)
Seab C. G., Shull J. M., 1983, ApJ, 275, 652
Shen X., Vogelsberger M., Nelson D., Tacchella S., Hernquist L., Springel V., Marinacci F., Torrey P., 2021, MNRAS, 510, 5560
Sheth R. K., Tormen G., 1999, MNRAS, 308, 119
Slavin J. D., Dwek E., Mac Low M.-M., Hill A. S., 2020, ApJ, 902, 135
Sommovigo L., Ferrara A., Carniani S., Zanella A., Pallottini A., Gallerani S., Vallini L., 2021, MNRAS, 503, 4878
Sommovigo L., Ferrara A., Pallottini A., Carniani S., Gallerani S., Decataldo D., 2020, MNRAS, 497, 956
Song M. et al., 2016, ApJ, 825, 5
Stark D. P., 2016, ARA&A, 54, 761
Temim T., Dwek E., Arendt R. G., Borkowski K. J., Reynolds S. P., Slane P., Gelfand J. D., Raymond J. C., 2017, ApJ, 836, 129
Tinsley B. M., 1980, Fund. Cosmic Phys., 5, 287
Todini P., Ferrara A., 2001, MNRAS, 325, 726
Triani D. P., Sinha M., Croton D. J., Pacifici C., Dwek E., 2020, MNRAS, 493, 2490
Vijayan A. P. et al., 2021, MNRAS, in press
Vijayan A. P., Clay S. J., Thomas P. A., Yates R. M., Wilkins S. M., Henriques B. M., 2019, MNRAS, 489, 4072
Watson D., Christensen L., Knudsen K. K., Richard J., Gallazzi A., Michałowski M. J., 2015, Nature, 519, 327

APPENDIX: COMPARISON OF THE DUST-TO-STELLAR MASS RELATION WITH OTHER SEMI-ANALYTIC MODELS

In addition to being a key output of our model, the dust-to-stellar mass relation is one of the key observables for the REBELS program. We now compare our results to those from a number of semi-analytic models including the Santa Cruz model (Popping et al. 2017), L-GALAXIES (Vijayan et al. 2019), and DUSTY SAGE (Triani et al. 2020) that are able to simulate a statistically significant number of galaxies covering the REBELS stellar mass range ($M_* \sim 10^9$–10^{10}M$_\odot$). While all these models include (varying) prescriptions of the key physical process of gas cooling, star formation, SN feedback, chemical enrichment, and dust (formation, astration, destruction, ejection, accretion), we caution they have been base-lined against low-redshift ($z \sim 0$) data as compared to our model that has been base-lined against all available observables at $z \gtrsim 5$.

The Santa Cruz model (Popping et al. 2017) predicts the largest dust mass values for a given stellar mass. Finding a dust-to-stellar mass ratio that increases from ~ 1 to 4 per cent as M_* increases from 10^9 to 10^{10}M$_\odot$, this model severely exceeds the average dust-to-stellar mass ratio of about 0.28 per cent found both by our model and by the REBELS program for $M_* \sim 10^{9.5-10}$M$_\odot$ galaxies. Indeed, this model sits at the upper limit for all the observed dust masses so far at $z \sim 7$. As discussed in Section 4.1, if such high dust masses were to be representative of the entire LBG population, the UV LF would be severely underpredicted due to dust attenuation unless this was compensated by intrinsically higher SFRs. Physically, these high dust masses are possibly driven by the high production rate density in this model as well as the fact that they allow smooth accretion of metal- and dust-rich gas. Interestingly, although the amplitude is higher, the slope from this model is in good agreement with ours.

We then show both the fiducial as well as the maximal model results from the L-GALAXIES model (Vijayan et al. 2019) that bracket the observed dust-to-stellar mass range. These authors assume all dust to be destroyed in major mergers in their fiducial model while we allow dusty mergers. Despite their different prescriptions for all key processes of galaxy formation, their fiducial model is only slightly lower than ours (by a factor of 2.5) with a very similar slope. Their maximal model (that assumes saturated grain growth and no destruction) also lies very close to our 'maximal dust mass' model

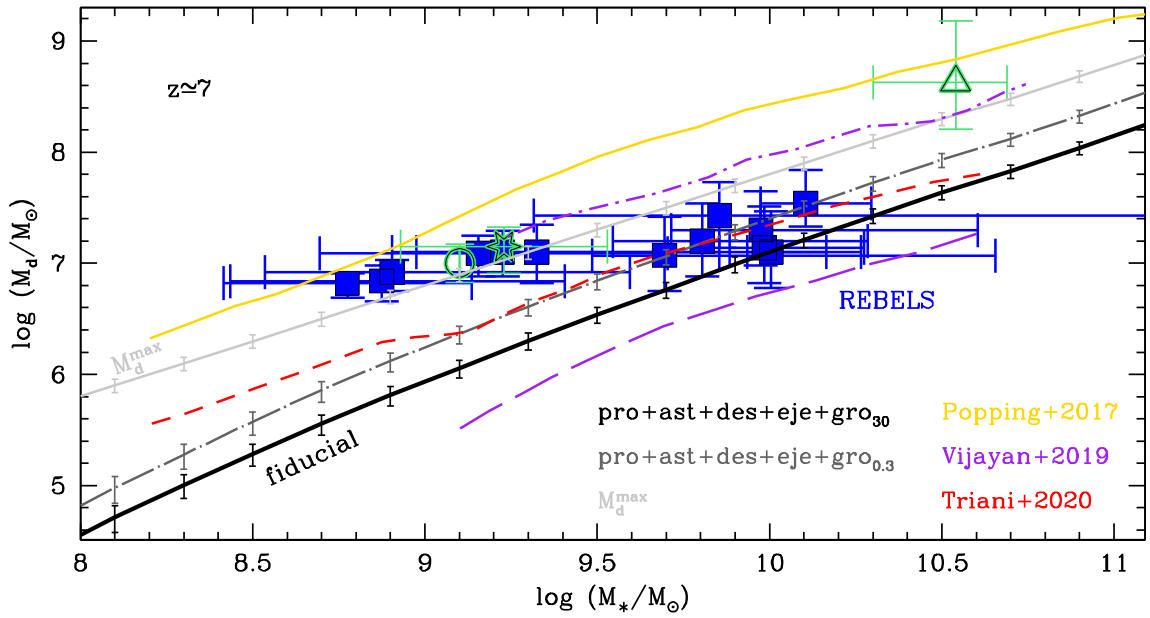

Figure A1. The dust mass as a function of stellar mass at $z \sim 7$. Solid blue points show data from REBELS (Bouwens et al. 2022) where the stellar and dust masses have been re-scaled to a Salpeter IMF with 0.1–100 $M_\odot$. The other points show observational data for A1689−zD1 (empty star) from Watson et al. (2015) and Bakx et al. (2021), for B14−65666 (empty circle) from Hashimoto et al. (2019) and for SPT0311-58 (empty triangle) from Reuter et al. (2020). The solid black, dot-dashed grey and solid grey lines (along with 1σ error bars) show results from this work for the *fiducial* model, a grain growth time-scale of 0.3 Myr and the 'maximal dust mass' model, respectively. These are compared to the results from three other semi-analytic models: The solid yellow line shows the fiducial model from Popping et al. (2017), the violet dashed and dot-dashed lines show the fiducial model and upper limits from Vijayan et al. (2019), and the red line shows the fiducial results from Triani et al. (2020).

that also ignores dust destruction and assumes grain growth on a 0.3-Myr time-scale compared to their 5×10^4 yr.

Finally, the results of the DUSTY SAGE model (that also uses the Dwek grain growth model but an ISM grain growth time-scale of 0.4 Myr) lie very close to our model that includes all the key dust process and where ISM grain growth takes place on a 0.3-Myr time-scale. This is quite heartening, given their very different prescriptions for star formation, SN feedback, and the fact that they too allow for accretion of metal- and gas-rich IGM gas (the 'galactic fountain' model). While this model provides the best fit as compared to the other two for observed $M_* \gtrsim 10^{9.5} M_\odot$ galaxies, as in our model, it underpredicts the dust masses for lower mass systems.

[1]*Kapteyn Astronomical Institute, University of Groningen, PO Box 800, NL-9700 AV Groningen, The Netherlands*
[2]*Scuola Normale Superiore, Piazza dei Cavalieri 7, I-56126 Pisa, Italy*
[3]*Leiden Observatory, Leiden University, NL-2300 RA Leiden, Netherlands*
[4]*Observatoire de Genève, CH-1290 Versoix, Switzerland*
[5]*Cosmic Dawn Center (DAWN), Niels Bohr Institute, University of Copenhagen, Jagtvej 128, DK-2200 København N, Denmark*
[6]*Astrophysics Research Institute, Liverpool John Moores University, 146 Brownlow Hill, Liverpool L3 5RF, UK*
[7]*Departmento de Astronomia, Universidad de Chile, Casilla 36-D, Santiago 7591245, Chile*
[8]*Centro de Astrofisica y Tecnologias Afines (CATA), Camino del Observatorio 1515, Las Condes, Santiago 7591245, Chile*
[9]*Centre for Astrophysics Research, Department of Physics, Astronomy and Mathematics, University of Hertfordshire, College Lane, Hertfordshire AL10 9AB, UK*
[10]*Hiroshima Astrophysical Science Center, Hiroshima University, 1-3-1 Kagamiyama, Higashi-Hiroshima, Hiroshima 739-8526, Japan*
[11]*Nucleo de Astronomia, Facultad de Ingenieria y Ciencias, Universidad Diego Portales, Av. Ejercito 441, Santiago, Chile*
[12]*Astrophysics, The Denys Wilkinson Building, University of Oxford, Keble Road, Oxford OX1 3RH, UK*
[13]*International Centre for Radio Astronomy Research, University of Western Australia, 35 Stirling Hwy, Crawley, WA 6009, Australia*
[14]*ARC Centre of Excellence for All Sky Astrophysics in 3 Dimensions (ASTRO 3D), Canberra, ACT 2601, Australia*
[15]*Research Institute for Science and Engineering, Waseda University, 3-4-1 Okubo, Shinjuku, Tokyo 169-8555, Japan*
[16]*National Astronomical Observatory of Japan, 2-21-1, Osawa, Mitaka, Tokyo, Japan*
[17]*Dipartimento di Fisica, Sapienza, Universita di Roma, Piazzale Aldo Moro 5, I-00185 Roma, Italy*
[18]*INAF/Osservatorio Astrofisico di Arcetri, Largo E. Femi 5, I-50125 Firenze, Italy*
[19]*Leiden Observatory, Leiden University, NL-2300 RA Leiden, The Netherlands*
[20]*Sterrenkundig Observatorium, Ghent University, Krijgslaan 281 – S9, B-9000 Gent, Belgium*
[21]*Department of Physics and Astronomy, University College London, Gower Street, London WC1E 6BT, UK*
[22]*I. Physikalisches Institut, Universität zu Köln, Zülpicher Strasse 77, D-50937 Köln, Germany*
[23]*INAF/Osservatorio Astronomico di Roma, via Frascati 33, I-00078 Monte Porzio Catone, Roma, Italy*
[24]*Sapienza School for Advanced Studies, Viale Regina Elena 291, I-00161 Roma Italy*
[25]*Istituto Nazionale di Fisica Nucleare, Sezione di Roma1, Piazzale Aldo Moro 2, I-00185 Roma, Italy*
[26]*Steward Observatory, University of Arizona, 933 N Cherry Ave, Tucson, AZ 85721, USA*

This paper has been typeset from a TEX/LATEX file prepared by the author.